

# Effect of different ions on dissolution rates of silica and feldspars at high pH

M. Bagheri<sup>a,\*</sup>, B. Lothenbach<sup>b</sup>, M. Shakoorioskooie<sup>b,c,d</sup>, K. Scrivener<sup>a</sup>

<sup>a</sup> Laboratory of Construction Materials, EPFL, 1015 Lausanne, Switzerland

<sup>b</sup> Concrete and Asphalt Laboratory, Empa, Swiss Federal Laboratories for Materials Science and Technology, CH-8600 Dübendorf, Switzerland

<sup>c</sup> Institute for Building Materials (IfB), ETH Zürich, CH-8093 Zürich, Switzerland

<sup>d</sup> Center for X-ray Analytics, Empa, Swiss Federal Laboratories for Materials Science and Technology, CH-8600 Dübendorf, Switzerland

## ARTICLE INFO

### Keywords:

Dissolution kinetics  
Silica  
Feldspar  
High pH  
Temperature

## ABSTRACT

The dissolution kinetics of silica-containing minerals in aggregates influences strongly the process of ASR in concrete. In this paper, the effect of different ions on the dissolution rates of SiO<sub>2</sub> (amorphous and quartz) and feldspars at high pH values was studied by following the increase of silicon concentrations in dissolution experiments and with a novel approach of measuring the evolution of scratches of polished surfaces. The second method avoided the problem of precipitation in some systems, such as the formation of C-S-H when calcium was present and lithium silicates in the presence of lithium. At high pH values, lithium, calcium and sulfate increased the dissolution rates of silica and feldspars, while iron, magnesium and additional NaCl, KCl or CsCl showed no significant effect. In contrast, aluminium slowed down significantly the dissolution rates of quartz, amorphous silica and Na and K-feldspar at for all temperatures studies: 20, 40 and 60 °C.

## 1. Introduction

Building materials play a key role in modern infrastructures and housing. Cement-based materials are in high demand because of their high performance, availability of raw materials, low cost, and relatively low environmental footprint per unit mass produced [1]. The durability of concrete structures can be affected by the so-called alkali silica reaction (ASR), which can cause expansion and deterioration of the concrete in the long term. With susceptible aggregates, the high pH of the pore solution of concrete can lead to the dissolution of silica within aggregates and to the formation of ASR products [2]. The formation of ASR products and thus the rate at which cracking occurs depends strongly on the dissolution rate of the reactive phases inside the aggregates [3]. In ASR-reactive aggregates, dissolution often initiates at grain boundaries, and in the amorphous or poorly crystalline forms of quartz and feldspars [2,4,5]. Dissolution of feldspar may accelerate dissolution reaction due to alkali release or slow it down due to the release of aluminium [6]. The dissolution kinetics of reactive aggregates in concrete depends on different factors including i) the composition of the pore solution, which depends on cement and aggregate composition [4,7], ii) surface area, crystallinity and presence of crystal defects in the reactive aggregates [3], iii) moisture [8] and iv) temperature [7,9,10].

The composition of the pore solution can be influenced by the type of cement and by the kind and amount of supplementary cementitious materials (SCMs) [11]. Not only the alkali concentrations and pH affect the dissolution kinetics of reactive aggregates but also the concentration of other ions such as aluminium in the pore solution. An improved understanding of the role of different ions is thus fundamental to develop efficient mitigation strategies to control ASR in concrete.

A possibility to lower the risk of damage due to ASR is to decrease the dissolution rate of silica-containing minerals within the aggregates, as the dissolution of metastable silica from aggregate is the initial reaction of ASR [12]. This goal can be achieved by the use of appropriate cement paste, which changes the pore solution composition. It has been shown that the presence of aluminium can slow down the dissolution kinetics of aggregates [13,14], while the dissolution increases with temperature, pH and alkali hydroxide concentration [5,9,15]. Also, the type of alkali also has been reported to affect dissolution [15–17]. The effect of other elements is less clear; contradictory findings exist as most studies have been carried out in the presence of cement and based on expansion measurements [18,19], which make it impossible to clearly identify the effect of one single element and to distinguish between the effect of an element on the dissolution kinetics and its effect on the kind and amount of ASR product formed. Systematic studies of dissolution kinetics of

\* Corresponding author.

E-mail addresses: [mahsa.bagheri@epfl.ch](mailto:mahsa.bagheri@epfl.ch) (M. Bagheri), [barbara.lothenbach@empa.ch](mailto:barbara.lothenbach@empa.ch) (B. Lothenbach), [mahdieh.shakoorioskooie@empa.ch](mailto:mahdieh.shakoorioskooie@empa.ch) (M. Shakoorioskooie), [karen.scrivener@epfl.ch](mailto:karen.scrivener@epfl.ch) (K. Scrivener).

<https://doi.org/10.1016/j.cemconres.2021.106644>

Received 24 May 2021; Received in revised form 15 October 2021; Accepted 15 October 2021

Available online 6 November 2021

0008-8846/© 2021 The Author(s). Published by Elsevier Ltd. This is an open access article under the CC BY license (<http://creativecommons.org/licenses/by/4.0/>).

minerals have been generally been carried out under acid to neutral pH conditions, where their effect is often different than at high pH values, while studies under high pH conditions are still rare. Therefore, a systematic study is needed to clarify the effect of the different ions such as Al, Li, Fe, Na, on the dissolution kinetics of reactive silica and feldspars.

Cement pastes with aluminium-rich SCMs such as fly ash or meta-kaolin have been observed to suppress expansion due to ASR [2,20,21]. Aluminium decreases the rate of dissolution of amorphous silica and quartz [14,22–24], and so the dissolution of aggregates [2,22]. This has been related to the tendency of aluminium to adsorb on silica surfaces, where it passivates the active silica sites and slows down further dissolution [13,14,25]. The sorption of aluminium tends to decrease with pH in the high pH range (>13) [2,14,22,25].

Some studies based on measurements of mass loss [26,27] or increase in silicon concentrations [28] have suggested that calcium in solution decreases the dissolution of silica due to the formation of C-S-H on the silica surface. However, the study of mass losses and dissolved concentrations in the presence of C-S-H precipitates makes the interpretation of such results challenging. Other studies at near neutral pH, where no C-S-H can form, have suggested an increase of quartz dissolution in the presence of calcium [16].

Lithium can prevent expansion due to ASR as shown by McCoy and Caldwell [29] in 1951 and confirmed in several studies [30–32]. The presence of lithium lowers the CaO/SiO<sub>2</sub> as well as the (Na + K)/Si ratio in the ASR products [31,32]. The amount and the availability of other alkalis (Na + K) and the type of aggregate determine the amount of lithium required to control the expansion due to ASR [18,29–31]. It has been suggested that, Li<sup>+</sup>, due to its smaller ionic radius and higher charge density, is more readily incorporated in ASR products than K<sup>+</sup> and Na<sup>+</sup> and that lithium-based ASR products are non-expansive [31,32]. Some studies suggested that lithium reduces silica dissolution compared to sodium or potassium [12,33,34], while others [15,16,28,35] observed no significant influence of Li in dissolution tests. It should be noted that lithium can precipitate as Li<sub>2</sub>SiO<sub>3</sub> [27], which again can make the interpretation of results based on silicon concentration or mass loss difficult. In addition, in the present research, the effect of sulfate on ASR expansion is studied, as high temperatures as often present during ASR tests increase sulfate concentrations in solution significantly [36,37], which could affect the dissolution kinetics.

Most studies of dissolution kinetics of minerals have been carried out under acid to neutral pH conditions, while studies under high pH conditions are rare, such that we lack a fundamental understanding of different factors affecting dissolution kinetics and their interplay. As a result, numerous questions are still open and there is a high degree of uncertainty in mitigation of ASR and prediction of expansion due to ASR.

The present study investigates the effect of solution composition on the dissolution kinetics of silica (amorphous silica and quartz) and feldspars (K-feldspar and Na-feldspar) at high pH values by studying i) indirectly by following the increase of silicon concentrations during dissolution experiments, ii) by observing mass changes and iii) directly the dissolution of scratched surfaces, as an innovative method.

## 2. Materials and methods

### 2.1. Mineral samples

The materials used were:

- amorphous silica: two powders with particle sizes 100–250 µm, and 100–360 µm, labelled (AmS-1 and AmS-2).
- quartz: two powders with particle sizes 100–250 µm, and 100–360 µm, labelled (Q-1 and Q-2).
- amorphous silica plates (diameter 25 mm and thickness 2 mm) with >99.9% purity from Lanno Quartz (Xinpu, China), labelled (AmS-Pl).

- albite (Na-feldspar): from Rantzaer Töpferbedarf (Barmstedt, Germany), labelled Alb-1,
- natural rocks containing mostly:
  - microcline (K-feldspar): labelled MicrocR,
  - orthoclase (K-feldspar) labelled OrthoR and
  - albite (Na-feldspar), labelled AlbR.

Powder samples (labelled Microc and Alb-2) were prepared from the rocks (MicrocR and AlbR), with a size fraction < 100 µm by crushing and sieving. In order to remove very fine particles, the powder samples were put in a glass beaker and cleaned ultrasonically with deionized water and isopropanol three times for few minutes, and dried at 40 °C before doing dissolution experiments.

X-ray fluorescence (XRF) and X-ray Powder Diffraction (XRD) were used to determine the chemical composition and crystalline structure of the materials used. The XRD patterns (between 5° to 70° 2θ during 30 min with a step size of 0.017°) were recorded using a PANalytical X'Pert Pro MPD diffractometer with CuKα<sub>1,2</sub> radiation. Quantification of the crystalline and amorphous fractions was done using Rietveld analyses. Alb-1 contained 88% and AlbR/Alb-2 82% of albite. OrthoR and MicrocR/Microc samples contain almost 50% of orthoclase and microcline; the non-crystalline content is most likely also feldspars with low crystallinity as feldspars were observed to be dominant phases using SEM/EDX. The amorphous silica samples, AmS-1/2 and AmS-Pl, showed no XRD peaks confirming amorphous structure, and Q-1 and Q-2 showed quartz (~94%) as detailed in Table 1 and in Fig. B1.

The specific surface area of quartz and amorphous silica powder was also measured using laser diffraction and N<sub>2</sub> adsorption. The laser diffraction measurement was impacted by sedimentation during the measurements, and the N<sub>2</sub> adsorption was not efficient as the materials were not porous. Therefore, to report comparable specific surface area values, SEM imaging was used to observe and calculate the specific surface area. The specific surface area was determined using 2-dimensional (2D) cross-section SEM images (Figs. A2 and A3) and presented in Table 1.

### 2.2. Exposure solutions

Table 2 summarises the solutions and storage temperatures used for the dissolution experiments. Sodium chloride (99.99%, Merck), caesium chloride (ultrapure 99.9%, Company abcr), lithium chloride (99.9%, APOLLO SCIENTIFIC), lithium hydroxide (98%, ACROS), iron (III) chloride hexahydrate (98%, Merck), magnesium chloride (99.9%, ACROS), calcium chloride (≥98%, RDTH), aluminium chloride anhydrous powder (99%, Aesar), aluminium nitrate nonahydrate (≥98.5, Merck), potassium hydroxide (≥85%, Fisher Chemical) and sodium hydroxide (≥98%, RDTH) were used to prepare the solutions together with ultra-pure water. The concentrations were selected based on the range of measured concentrations in the pore solution of cement pastes and mortars [11]. In the case of Al, Mg, Ca and Fe an upper concentration of 3 mM was used, to ensure an as high as possible concentration, although in the case of Ca, Mg and Fe the final concentrations were lower due to the precipitation of C-S-H, brucite and iron hydroxide, comparable to the concentrations in cement pore solutions.

### 2.3. Dissolution measurements

The dissolution of a solid can be followed by the amount of ions released to the surrounding solutions or by following its mass change, or by the novel technique developed in this project, the scratch tracking method, where the evolution of the surface is measured directly.

#### 2.3.1. Dissolution by scratch tracking

The increase in width of scratches at the surface during dissolution was determined using an innovative “scratch-tracking” method based on changes observed in SEM images over time, as introduced for the first

**Table 1**

Phase analysis of the materials used for dissolution experiments.

Technique	Component	Alb-1 <sup>a</sup>	AlbR/Alb-2 <sup>b</sup>	OrthoR <sup>c</sup>	MicrocR/Microc <sup>d</sup>	AmS-1 <sup>e</sup>	AmS-2 <sup>f</sup>	Q-1 <sup>g</sup>	Q-2 <sup>h</sup>
XRF (wt%)	SiO <sub>2</sub>	69.6	–						
	Al <sub>2</sub> O <sub>3</sub>	18.6							
	Na <sub>2</sub> O	10.4							
XRD (wt%)	Quartz: SiO <sub>2</sub> [ICSD 174]	7.6	–			–		93.9	
	Cristobalite: SiO <sub>2</sub> [ICSD 75300]	–						0.2	
	Coesite: SiO <sub>2</sub> [ICSD 18112]	–						2.8	
	Feldspar: Albite: NaAlSi <sub>3</sub> O <sub>8</sub> [ICSD 37653]	88.2	82.0	–	13.2			–	
	Feldspar: Microcline: KAlSi <sub>3</sub> O <sub>8</sub> [ICSD 83531]	–			48.8				
	Feldspar: Orthoclase: KAlSi <sub>3</sub> O <sub>8</sub> [ICSD 10270]	–		52.4	8.2				
	Feldspar: Sanidine: K(AlSi <sub>3</sub> O <sub>8</sub> ) [ICSD 10274]	–		10.9	–				
	Lawsonite: CaAl <sub>2</sub> Si <sub>2</sub> O <sub>7</sub> (OH) <sub>2</sub> ·H <sub>2</sub> O [COD 9010839]	–	17.0	–					
	Amorphous/non-crystalline	4.2	1.1	36.8	30.1	100		3.1	
		48 ± 12	42 ± 27	–	51 ± 28	10 ± 3	5 ± 3	15 ± 1	17 ± 2
Specific S.A. (m <sup>2</sup> /kg) <sup>i</sup>	–								

<sup>a</sup> Albite from Rantzaer Töpferbedarf (Barmstedt, Germany).<sup>b</sup> Albite natural rock, from Navarro River, Mendocino Co, California. Albite composition: Na<sub>0.95</sub>K<sub>0.05</sub>AlSi<sub>3</sub>O<sub>8</sub> [38].<sup>c</sup> Orthoclase natural rock, from Breckenridge, Colorado, USA.<sup>d</sup> Microcline natural rock (amazonite), from Brazil.<sup>e</sup> Amorphous silica (100–250 μm).<sup>f</sup> Amorphous silica (100–360 μm).<sup>g</sup> Quartz (100–250 μm).<sup>h</sup> Quartz (100–360 μm).<sup>i</sup> The specific S.A. was measured on powder samples with size fraction < 100 μm for Alb-2 and Microc, used for dissolution experiments. The errors show the standard deviation of the values.**Table 2**

Summary of solutions and storage temperatures for dissolution experiments.

Solution				Storage temperature (°C)
Alkaline solution	Element	Initial concentrations (mM)	Salt	
100 or 400 mM KOH	–			20, 40, 60
400 mM NaOH				40
100 mM KOH	Al	1, 3	AlCl <sub>3</sub> or Al (NO <sub>3</sub> ) <sub>3</sub> ·9H <sub>2</sub> O	20, 40
400 mM KOH		0.1, 0.3, 0.5, 1, 3		40, 60
	Ca	3 <sup>a</sup>	CaCl <sub>2</sub>	
	Li	10, 40, 100, 400	LiCl or LiOH	
	Sulfate	200	K <sub>2</sub> SO <sub>4</sub>	40
	Sulfate + Al	50 + 3	K <sub>2</sub> SO <sub>4</sub> and AlCl <sub>3</sub>	
	Fe	3 <sup>b</sup>	FeCl <sub>3</sub>	40, 60
	Mg	3 <sup>b</sup>	MgCl <sub>2</sub>	
	Na	400	NaCl	
	K	400	KCl	40
	Cs	400	CsCl	40, 60

<sup>a</sup> The solubility of Ca is limited at high pH due to the precipitation of portlandite (Fig. E1). The 3 mM CaCl<sub>2</sub> chosen corresponds also to Ca concentrations typically observed in the pore solution of cement pastes [11].<sup>b</sup> Note that the initial and final concentrations in the case of Mg and Fe were below the detection limit of 0.5 mg/L due to the precipitation of brucite and iron hydroxide at the high pH of the experiment and/or using highly diluted solutions for ICP-OES measurements as high alkali content could damage the machine.

time in our recent research [39]. The impregnated samples (Q-1, MicrocR, OrthoR, AlbR) were polished to 1/4 μm, carbon coated and analyzed by SEM (secondary electron (SE) detector, HV of 2/3 kV, WD of 5.0/6.0 mm, magnification of 5000×, aperture size of 30.00 μm, image size of 1024 × 1536 pixels with an individual pixel size of 5.43 × 5.43 nm<sup>2</sup> to collected the images) and SEM/EDX (backscattered electron (BSE) detector, HV of 12 kV, WD of 8.5 mm, aperture size 60.00 μm to analyze the chemical composition of the minerals) in at least four different areas to assess the chemical composition and the amount of scratches. SEM images were collected before and after dissolution in different solutions at 40 °C for 21 days; the carbon coating was removed before dissolution gently by polishing for 2 to 3 min using a soft polishing cloth (OP-Nap, Struers) and petroleum lubricant. After dissolution, the samples were washed gently with ultra-pure water and isopropanol to remove any precipitate and dried at 40 °C for 1 day before a reanalysis of the samples by SEM.

In order to quantify the effect of dissolution on the widening of the polishing-scratches, SEM images, taken after dissolution (21 days), were spatially aligned with their corresponding SEM images before dissolution, using a “rigid body registration” algorithm, implemented at SimpleElastix image registration library (provided by Insight Segmentation and Registration Toolkit (ITK), using Python interface, as our previous research [39]). The scratches in both SEM images (before and after dissolution) were segmented by applying a threshold using Avizo software (by Thermo Fisher Scientific). The scratch surface area fraction (SSAF<sub>i</sub>(%)) for each segmented binary scratch image (please see more information in Appendix A, Surface area of the segmented binary scratches) was computed by the same software (Aviso) based on the following equation:

$$SSAF_i(\%) = \frac{\text{surface area of the segmented binary scratches}}{\text{surface area of the SEM image}} \quad (1)$$

where  $i$  indicates the time at which the SEM image was acquired. Finally, the absolute change of scratch surface area fraction ( $\Delta SSAF(\%)$ ) due to the dissolution was calculated by:

$$\Delta SSAF(\%) = SSAF_a(\%) - SSAF_b(\%) \quad (2)$$

where  $SSAF_b(\%)$  is the scratch surface area before exposure and  $SSAF_a(\%)$  is the scratch surface area after exposure in alkaline solution.

For each dissolution condition, the  $\Delta SSAF(\%)$  was computed on at least three SEM-image sets and the average of all values along with corresponding standard deviations is reported.

### 2.3.2. Dissolution in dilute solutions

To follow the dissolution, the increase of Si concentration in solution over time was followed in solutions for the solids (AmS-1/2, Q-1/2, Alb-1/2, Microc). For each experiment, 500 mL of solution were placed in a polypropylene container [40] (at 20 or 40 °C) or a teflon container (PTFE container from Fisherbrand™) (at 60 °C) with 0.5 g of powder, resulting in a solution to solid ratio of 1000 mL/g, following the procedure detailed in [40]. The use of high water to solid ratio minimizes the precipitation of secondary phases during the dissolution experiments. Potassium or sodium hydroxide solutions with additions of different chloride salts were used as summarised in Table 2. At each sampling time (almost after 1–2 months), 3 mL of the solution was collected and filtered (0.2 µm nylon filter). The concentration of Si released as a function of time was measured on subsamples diluted by a factor of 10 by Inductively Coupled Plasma Optical Emission Spectrometry (ICP-OES; Shimadzu ICPE-9000) or ion chromatography (IC; Dionex DP ICS-3000). The pH was measured on another aliquot of the solution with a BlueLine 14 pH electrode (SI Analytics) and a Lab 850 pH meter considering the calibration curve of KOH solutions (0.1, 0.2, 0.5 and 1 M KOH) as detailed in [41] and [39]. All pH values in the present paper were measured at lab temperature (23–24 °C) and corrected back to the original temperature of the experiments, i.e. by deducting 0.47 pH units at 40 °C and 0.99 at 60 °C as the pH measurement as well as the water ionization product are strongly dependent on temperature [42]. The correction of 0.47 pH units for 40 °C and 0.99 for 60 °C were calculated with GEMS for a 400 mM KOH solution [43].

The geochemical software GEMS [43] together with the PSI-nagra thermodynamic database [44], a cement specific database, Cemdata18 [45], and the thermodynamic data from Helgeson et al. [46] for albite and K-feldspar was used to calculate undersaturation with respect to amorphous silica, quartz, albite and K-feldspar in the solutions and potential oversaturation with respect to C-S-H. The saturation index (SI) of the different solids corresponds to:  $SI = \log IAP/K_{so}$ , where  $K_{so}$  represents the theoretical solubility product of the respective solid and IAP the ion activity product calculated based on the measured pH values and concentrations of Al, Ca, Si, K, and Na in solution. A positive saturation index ( $>0$ ) indicates that the solution is oversaturated with respect to this solid phase and this phase could possibly precipitate, while a negative value indicates undersaturation.

The Si release rate from silica or feldspars,  $r_{si}$ , in  $\text{mol}/(\text{m}^2 \cdot \text{s})$ , was obtained from the slope of the curve of the normalized concentration (taking into account solution volume, mass of solid and specific surface area) of measured Si versus time, as summarised in Eq. (3) for steady-state dissolution regime and linear trend:

$$r_{si} = \frac{d(X)}{\Delta t} \times \frac{1}{m \times S \times V_{sol}} \quad (3)$$

where  $\frac{d(X)}{\Delta t}$  is the change in Si concentration in mol/L within the considered time period in seconds,  $m$  is the mass of solid,  $V_{sol}$  is solution volume, and  $S$  corresponds to the initial specific surface area of the powder. Note that the dissolution rates strongly depend on the surface

area and particle geometry [47,48]. All error bars were calculated with respect to a 95% confidence interval (the difference between the rates, i) calculated from the best trend linear line and ii) the worse trend linear line divided by 2 determined the error of the rate calculations). The solid was collected at the end of dissolution experiments using filter paper 2 µm under vacuum, washed with isopropanol and deionized water and dried at 40 °C and analyzed using XRD.

### 2.3.3. Dissolution based on mass loss

In a further series of experiments, the mass changes of an amorphous silica plate (AmS-PI) were studied after immersion in 50 mL of 400 mM KOH solution without and with 3 mM  $\text{CaCl}_2$  or 400 mM LiCl at 60 °C. The plates were cleaned ultrasonically using isopropanol for few minutes and dried at 40 °C before exposure. The mass of each plate was recorded before exposure ( $mb$ ). After 7 months of reaction, the plates were cleaned with water and isopropanol to remove the precipitation and dried at 40 °C for few hours; the plates were weighted again after exposure ( $ma$ ). The remaining mass (%) for each plate was calculated using the following equation:

$$\text{Remaining mass}(\%) = \frac{ma}{mb} \times 100 \quad (4)$$

The mean of measurement for at least two different plates is reported. The error bars show the standard deviation of the values. A newly formed solid in the presence of 3 mM  $\text{CaCl}_2$  or 400 mM LiCl was collected using a filter paper 2 µm under vacuum, washed with isopropanol and ultra-pure water and dried at 40 °C, before their characterization by XRD.

## 3. Results

### 3.1. The effect of pH and temperature on $\text{SiO}_2$ dissolution

Fig. 1 shows the increase of Si concentration, released from 0.5 g of amorphous silica with a size fraction of 100 to 250 µm (filled circles) and 100 to 360 µm (circles with a cross) in 400 mM KOH as a function of time. The higher Si concentration observed for the finer amorphous silica underlines the need to normalize the measured Si concentration to the specific surface area of the solid, based on Eq. (3). Based on the slope of the curves and the surface area as detailed in Table 1, the calculated dissolution rates of AmS-1 ( $261 \pm 26$ )  $\times 10^{-9}$  and AmS-2 ( $242 \pm 29$ )  $\times 10^{-9}$   $\text{mol}/(\text{m}^2 \cdot \text{s})$  are comparable with a difference of  $<8\%$ . A second

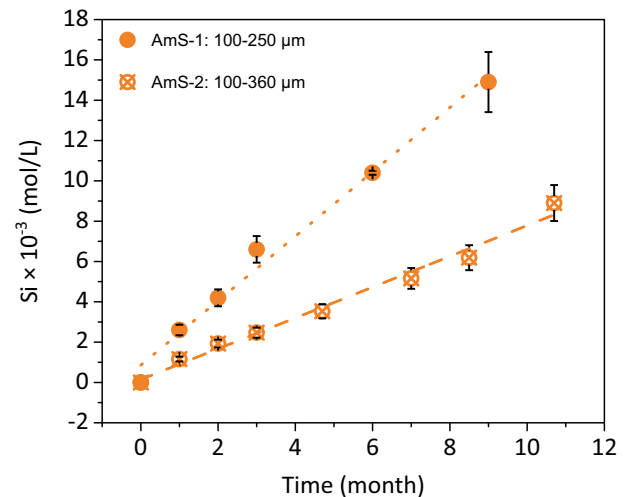
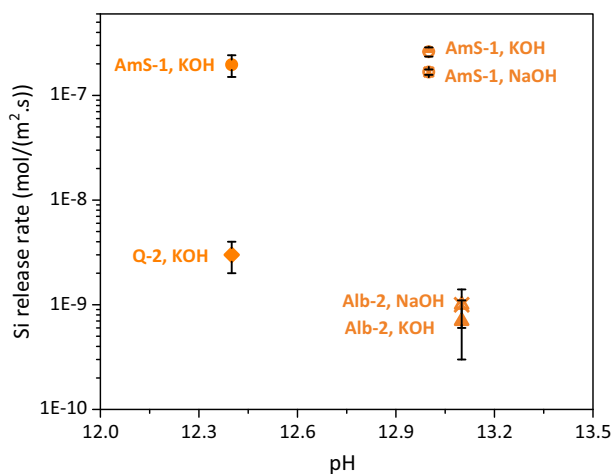
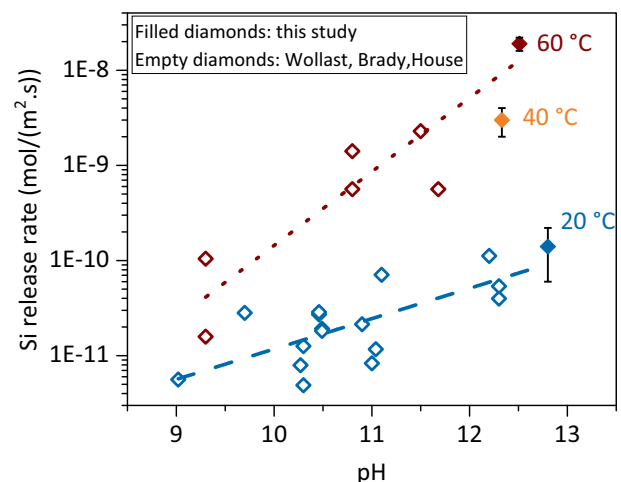


Fig. 1. The amount of released Si (mol/L) from 0.5 g of amorphous silica with two different size fractions (AmS-1: 100 to 250 µm and AmS-2: 100 to 360 µm) in 0.5 L of 400 mM KOH as a function of time at 40 °C. The error bars indicate the 10% measurement error of ICP-OES.

**Table 3**

Dissolution rates of quartz (Q), amorphous silica (AmS), albite (Alb) and microcline (Microc) in different solutions.

Solid	Solution			pH <sup>a</sup>		Storage temperature (°C)	Experiment duration (month)	$r_{Si} \times 10^{-9}$ (mol/ (m <sup>2</sup> .s)) <sup>b, g</sup>
	Alkaline solution	Initial concentrations (mM)	Salt	Initial	Final			
Q-1	400 mM KOH	–		12.5	12.5	60	19.7	19 ± 3
AmS-1				13.0	13.0	40	8.8	261 ± 26
					13.0		8.5	250 ± 47
AmS-2				12.9	12.9		14.2	242 ± 29
Alb-1				13.0	12.9		14.2	2 ± 0.5 <sup>c</sup>
Alb-2				13.0	13.1		12	0.7 ± 0.4
Microc				13.0	13.1		12	0.5 ± 0.4
Calcium	400 mM KOH	3	CaCl <sub>2</sub>	12.5	12.5	60	19.7	<2 <sup>d</sup>
Q-1				12.9	13.0	40	8.8	151 ± 58 <sup>e</sup>
AmS-1	400 mM KOH	40	LiCl	12.4	12.4	60	19.7	30 ± 3 <sup>f</sup>
Q-1				12.5			19.7	26 ± 2 <sup>f</sup>
AmS-2				12.9	12.8	40	14.2	261 ± 28 <sup>f</sup>
AmS-1				13.0	13.0		8.8	255 ± 28 <sup>f</sup>
AmS-2				12.9	12.8		14.2	191 ± 22 <sup>f</sup>
AmS-1				13.0	13.0		8.8	145 ± 26 <sup>f</sup>
Alb-2				13.0	13.2		12	0.9 ± 0.6 <sup>f</sup>
Microc				13.0	13.2		12	0.6 ± 0.4 <sup>f</sup>
Alb-1				12.9	12.8		14.2	2 ± 0.5 <sup>f</sup>
							14.2	3 ± 0.6 <sup>f</sup>
Sulfate								
AmS-1	400 mM KOH	200	K <sub>2</sub> SO <sub>4</sub>	13.0	13.0	40	10	197 ± 24
		3 + 50	AlCl <sub>3</sub> + K <sub>2</sub> SO <sub>4</sub>				12.4	65 ± 5

<sup>a</sup> The pH values were measured at the experiment temperatures.<sup>b</sup> Si concentrations were measured using ICP-OES.<sup>c</sup> Higher dissolution rate, as Alb-1 contains in addition 8% of quartz.<sup>d</sup> Precipitation of C-S-H is strongly probable.<sup>e</sup> Precipitation of C-S-H observed.<sup>f</sup> Precipitation of Li<sub>2</sub>SiO<sub>3</sub> is strongly probable, observed after 5 months of amorphous silica plate dissolution in 400 mM KOH + 400 mM LiCl at 60 °C.<sup>g</sup> All error bars were calculated with respect to a 95% confidence interval.**Fig. 2.** The Si release rate (mol/(m<sup>2</sup>.s)) from amorphous silica (AmS-1), quartz (Q-2) and albite (Alb-2) in different solutions at 40 °C (pH values were measured at 40 °C). All error bars were calculated with respect to a 95% confidence interval.**Fig. 3.** The Si release rate (mol/(m<sup>2</sup>.s)) of quartz (Q) from literature: Wollast and Chou [49]; Brady and Walther [50] and House and Orr [51] (empty diamonds) and the results of this study for quartz (Q-1/2) (filled diamonds) at different temperatures (20–25, 40 and 60 °C) as a function of pH (pH values were reported at the experimental temperatures). The blue color indicates experiments at 20–25 °C, orange at 40 °C and dark red at 60 °C. All error bars for the dissolution rates of the present study were calculated with respect to a 95% confidence interval. (For interpretation of the references to color in this figure legend, the reader is referred to the web version of this article.)



experiment on AmS-1 resulted in the same dissolution rate  $250 \pm 47 \times 10^{-9} \text{ mol}/(\text{m}^2\cdot\text{s})$ , indicating good repeatability of the measurements and a total (experimental and systematic) error of <5% (Table 3).

The dissolution of amorphous silica in 400 mM of NaOH at 40 °C (circles with a cross) is  $167 \pm 10 \times 10^{-9} \text{ mol}/(\text{m}^2\cdot\text{s})$ , around two-thirds of the rate than in 400 mM KOH (half-filled circle) as shown in Fig. 2, in agreement with observations reported for quartz and silica [16,34]. The effect of pH on silica dissolution is relatively small between pH 12.4 (filled circle) and 13.0 (half-filled circle); the difference is within the error range. Although quartz and amorphous silica have the same chemical composition, the results at 40 °C indicated amorphous silica dissolves almost 10 times faster than quartz at high pH due to the effect of crystallinity on dissolution rate.

Albite dissolves at a similar rate in 400 mM of KOH (filled triangle,  $0.7 \pm 0.4 \times 10^{-9} \text{ mol}/(\text{m}^2\cdot\text{s})$ ) as in NaOH (triangle with cross sign symbol,  $1 \pm 0.4 \times 10^{-9} \text{ mol}/(\text{m}^2\cdot\text{s})$ ), indicating the effect of the alkali ion is negligible (Table 3).

Temperature, as well as high pH values, accelerate the dissolution rate of quartz as illustrated in Fig. 3. Both literature data, as well as our measurements, show a strong increase of dissolution rate with temperature.

Literature data [5] show a comparable increased dissolution rate at higher pH values also for albite (Na-feldspar) and K-feldspar as illustrated in Fig. 4. At 25 °C, the reported dissolution rate of albite is similar to the dissolution rate of quartz, while K-feldspar has a slower dissolution rate. In contrast, our results at 40 °C indicate a very similar dissolution rate for Na-feldspar (albite; alb-1/2) and K-feldspar (microcline), while quartz has slightly a higher dissolution rate. Note, however, that we observe for the sample alb-1, which contains in addition to albite also 8% of quartz, a dissolution rate similar to quartz, underlining that all minerals present may contribute to the observed Si-release rate. Thermodynamic calculations based on the measured and estimated concentrations as given in Table C1 confirmed that all the solutions studied were strongly undersaturated (saturation indices < 4) with respect to amorphous silica, quartz or feldspar until the end of the experiments (Fig. C1).

The measured dissolution rates of feldspar and quartz are very similar and a factor of 10 to 100 higher than the dissolution rates reported for muscovite, kaolinite, biotite, ... [5]: This difference in measured dissolution rates of different minerals is in agreement with our previous work which showed higher dissolution rates of quartz and feldspars in comparison with muscovite [39]. The large error bar in this figure is due to the very slow dissolution rate for feldspars, such that only a few measurements were above the detection limit of Si in the 14 months of the dissolution experiment.

### 3.2. Effect of aluminium on the dissolution rate of silica and feldspars

#### 3.2.1. Dissolution in diluted solution

Fig. 5 shows the Si release rate ( $\text{mol}/(\text{m}^2\cdot\text{s})$ ) from amorphous silica (AmS-1) as a function of Al concentration in KOH solution at pH 12.4 and 13.0. In solutions without Al the release rates are very similar at both pH values, but are considerably lower in the presence of dissolved Al. At pH 13.0, the presence of 1 mM of Al in solution decreased the amorphous silica dissolution rate 2 times; the lowest dissolution rate (4 times lower) was observed in the presence of 3 mM Al. At pH 12.4, the effect was even more clear (9 times lower) in the presence of 1 mM Al and by a factor of 18 in the presence of 3 mM Al. The presence of different counter anions (chloride or nitrate) did not affect the dissolution rates (see Fig. D1, Table 4; AmS-1 and AmS-2 in 400 mM KOH with 3 mM  $\text{AlCl}_3$  or  $\text{Al}(\text{NO}_3)_3$ ). This stronger inhibition of silica dissolution at lower pH values is consistent with the observations and calculations of Chappex and Scrivener [14,22]. Lower pH values increase the tendency of Al to sorb on silica (Fig. E1).

The dissolution of quartz and albite, shown in Fig. 5, is also lowered in the presence of Al. The effect of Al was stronger at 40 °C than 60 °C;

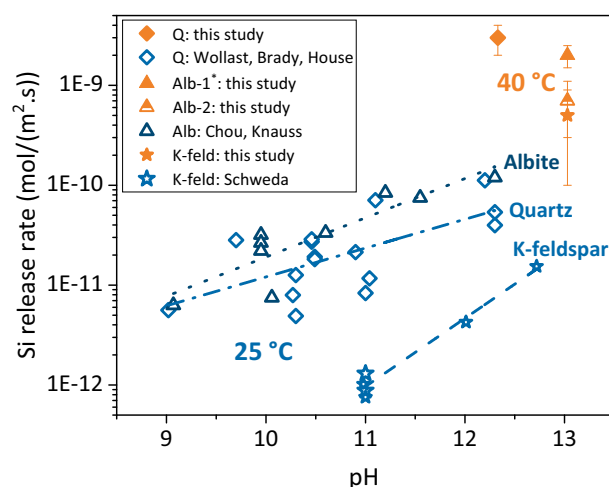


Fig. 4. The Si release rate ( $\text{mol}/(\text{m}^2\cdot\text{s})$ ) of quartz (Q), albite (Alb-1/Alb-2) and K-feldspar (K-feld) from literatures (empty dots) at 25 °C [5,49–54] and the results of this study (filled dots) at 40 °C as a function of pH. \* Higher dissolution rate, as Alb-1 contains in addition 8% of quartz. All error bars for the dissolution rates of the present study were calculated with respect to a 95% confidence interval.

the addition of 3 mM of Al decreased the dissolution rate of quartz by a factor of 200 times at 40 °C while at 60 °C 5 times lower dissolution rate was observed. The effect of aluminium was weaker in the case of albite.

#### 3.2.2. Surface changes during dissolution

The effect of Al on the dissolution was also followed by SEM and the progress of dissolution was quantified based on the changes in the width of existing scratches as illustrated in Fig. 6 for albite. The extent of pre-scratching was comparable for all the samples of albite as summarised in Fig. F1. A distinct growth of pre-existing scratches is observed in the presence of KOH alone, while much lesser changes are observed in samples with an addition of 3 mM of  $\text{AlCl}_3$ , confirming the observations discussed above.

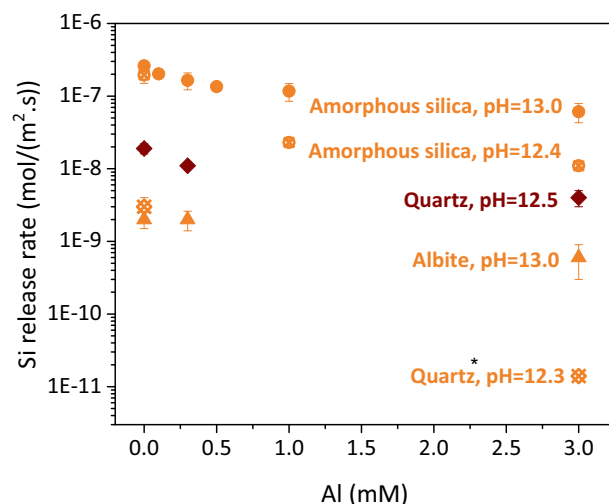


Fig. 5. Si release rate ( $\text{mol}/(\text{m}^2\cdot\text{s})$ ) from amorphous silica (AmS-1 at 40 °C), quartz (Q-1 at 60 °C (dark red filled diamonds), Q-2 at 40 °C (orange diamonds with cross sign symbols)) and albite (Alb-1 at 40 °C (orange filled triangles)) as a function of Al concentration in pH 12.3 to 13 (pH values were measured at the experiment temperatures). \* The dissolution rate is less than this number. All error bars were calculated with respect to a 95% confidence interval. (For interpretation of the references to color in this figure legend, the reader is referred to the web version of this article.)

**Table 4**

Dissolution rates of quartz, amorphous silica and albite in different solutions.

Solid	Solution			pH <sup>a</sup>		Storage temperature (°C)	Technique	Experiment duration (month)	r <sub>Si</sub> × 10 <sup>−9</sup> (mol/(m <sup>2</sup> ·s)) <sup>c</sup>
	Alkaline solution	Concentration (mM)	Salt	Initial	Final				
Q-1	400 mM	–		12.5	12.5	60	ICP-OES	19.7	19 ± 3
AmS-1	KOH			13.0	13.0	40		8.8	261 ± 26
Alb-2				13.0	13.1			12	0.7 ± 0.4
Alb-1				13.0	13.1			14.2	2 ± 0.5 <sup>b</sup>
Q-2	100 mM	–		12.9	12.8	20	IC	40	0.1 ± 0.08
	KOH			12.3	12.4	40		15	3 ± 1
AmS-1				12.4			ICP-OES	8.5	196 ± 46
AmS-1	400 mM	–		13.0	13.0	40	ICP-OES	12.4	167 ± 10
Alb-2	NaOH			13.0	13.1			12	1 ± 0.4
Aluminium									
Q-2	100 mM	3	Al	12.8	12.8	20	IC	40	<0.006
	KOH		(NO <sub>3</sub> ) <sub>3</sub> ·9H <sub>2</sub> O	12.3	12.3	40		15	<0.01
AmS-1		1	AlCl <sub>3</sub>	12.4	12.3		ICP-OES	8.5	23 ± 2
		3						8.5	11 ± 1
Q-1	400 mM	0.3		12.4	12.5	60		19.7	11 ± 1
	KOH	3			12.4			19.7	4 ± 1
AmS-1		0.1		13.0	13.0	40		8.8	202 ± 20
		0.3		12.9	12.9			8.8	165 ± 43
		0.5			13.0			8.8	135 ± 17
		1						8.8	117 ± 32
		3						12	61 ± 18
AmS-2			Al		12.9			14.2	55 ± 8
Alb-1		0.3	(NO <sub>3</sub> ) <sub>3</sub> ·9H <sub>2</sub> O	12.9	12.9			14.2	2 ± 0.6
		3						14.2	0.6 ± 0.3
Iron, magnesium									
Q-1	400 mM	3	FeCl <sub>3</sub>	12.4	12.5	60	ICP-OES	19.7	29 ± 3
AmS-1	KOH			12.9	12.9	40		8.8	314 ± 74
Q-1	400 mM	3	MgCl <sub>2</sub>	12.4	12.5	60	ICP-OES	19.7	26 ± 3
AmS-1	KOH			12.9	12.9	40		8.8	286 ± 71
Extra alkalis; sodium, potassium, caesium									
Q-1	400 mM	400	NaCl	12.5	12.4	60	ICP-OES	19.7	28 ± 2
AmS-1	KOH			13.0	13.0	40		8.8	260 ± 62
AmS-1	400 mM	400	KCl	13.0	13.0	40	ICP-OES	10	207 ± 21
	KOH								
Q-1	400 mM	400	CsCl	12.5	12.4	60	ICP-OES	19.7	24 ± 2
AmS-1	KOH			13.0	12.9	40		8.8	183 ± 14
Alb-2				13.0	13.1			12	1 ± 0.8

<sup>a</sup> The pH values were measured at the experiment temperatures.<sup>b</sup> Higher dissolution rate, as Alb-1 contains in addition 8% of quartz.<sup>c</sup> All error bars were calculated with respect to a 95% confidence interval.

The quantification (Fig. 7) showed a lower increase and thus less dissolution in the presence of KOH + 3 mM AlCl<sub>3</sub> than in the presence of KOH alone. Table F1 shows an example of values using the scratch-tracking method. For all four samples 3 mM Al decreased the dissolution rate, which is in good agreement with the results from the dissolution experiments discussed above as well as with literature data which indicated that Al in mmolar concentrations slows down the dissolution of silica [14,22], and silica-rich glasses [40].

In 400 mM KOH, both microcline and orthoclase (two different crystalline structures of K-feldspar) show a comparable surface reaction rate to quartz, while Na-feldspar (albite) showed slightly slower dissolution. In the presence of Al, the differences were small.

The results of the dissolution experiments and the increase of surface scratches underline both that Al slows down the dissolution rate of silica, quartz and feldspars, and that the effect is stronger at lower pH values.

This slower dissolution can be expected to inhibit ASR in cement pastes with aluminium-rich SCMs such as fly ash or metakaolin [2,20,21].

### 3.3. Effect of calcium on the dissolution rate of silica and feldspars

#### 3.3.1. Dissolution by scratch tracking

Scratch tracking in the presence of 3 mM CaCl<sub>2</sub> showed a clear increase of dissolution of quartz, microcline, orthoclase and albite as summarised in Fig. 8. This increased dissolution is in agreement with observations of Dove [15,16], who observed a clear increase of quartz dissolution in the presence of up to 10 mM calcium. This has been related to the tendency of Ca<sup>2+</sup> to form monodentate surface complexes [15,16] on silica, which can accelerate dissolution kinetics [55].

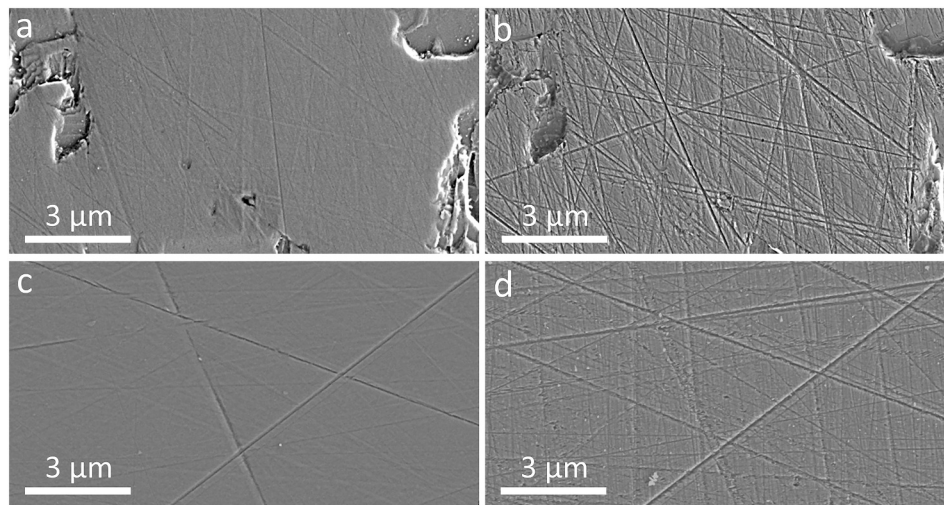


**Fig. 6.** Aligned SEM secondary electron images of albite (AlbR) to quantify the width changes of scratches over time; (a and c) before dissolution, and after 21 days of dissolution in (b) 400 mM KOH and (d) 400 mM KOH + 3 mM  $\text{AlCl}_3$  at 40 °C.

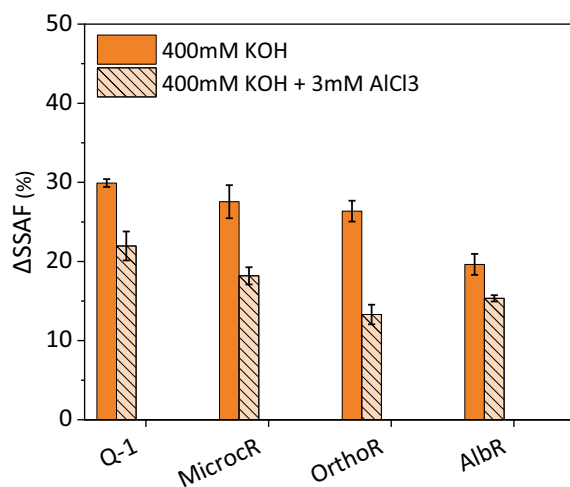


**Fig. 7.** The change of the scratch surface area ( $\Delta\text{SSAF}$ , %) of Q-1, Microcr, OrthoR and AlbR after 21 days of dissolution in 400 mM KOH and 400 mM KOH + 3 mM  $\text{AlCl}_3$  at 40 °C. The error bars show the standard deviation of the values.

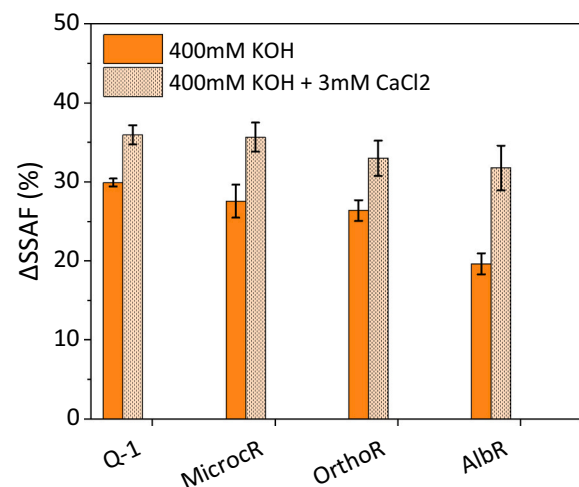


**Fig. 8.** The change of the scratch surface area ( $\Delta\text{SSAF}$ , %) of quartz (Q-1), microcline (Microcr), orthoclase (OrthoR) and albite (AlbR) after 21 days of dissolution in 400 mM KOH and in 400 mM KOH + 3 mM  $\text{CaCl}_2$  at 40 °C. The error bars show the standard deviation of the values.

### 3.3.2. Dissolution in diluted solution

In contrast to the increase of scratched surface observed in the presence of Ca, the dissolution study in diluted solutions indicated an apparent decrease in dissolution rates for amorphous silica and for quartz (Table 3). However, SEM and XRD clearly show the formation of C-S-H (Fig. 9) during the experiment. Thus, the slower increase of the measured Si concentrations does not mirror the dissolution rate of the amorphous silica and quartz, but rather the equilibrium between  $\text{SiO}_2$  dissolution and C-S-H precipitation, making the calculated dissolution rates meaningless.

In addition, the upper limit of saturation indices with respect to C-S-H was calculated using GEMS based on the measured Si concentrations and using the initial Ca concentrations (as the final Ca concentrations were below the detection limit. These upper limit saturation indices

indicated that the Ca-containing solutions were near saturation with respect to C-S-H ( $\text{SI} \approx -0.3$  to  $-0.5$ ).

### 3.3.3. Dissolution based on mass loss

The dissolution of amorphous silica was also followed by the decrease of the mass of plates immersed in 400 mM KOH without and with 3 mM  $\text{CaCl}_2$ , see Fig. 10. The remaining mass of the samples with Ca was slightly lower than those samples exposed to KOH only, confirming the observation of the surface changes. Note that as the samples were washed with isopropanol and de-ionized water so some C-S-H can be removed from the sample surface. However, under these conditions, the formation of C-S-H was still observed by XRD (Fig. G1), indicating a possibly even larger mass loss of  $\text{SiO}_2$  in the presence of C-S-H. Table G1



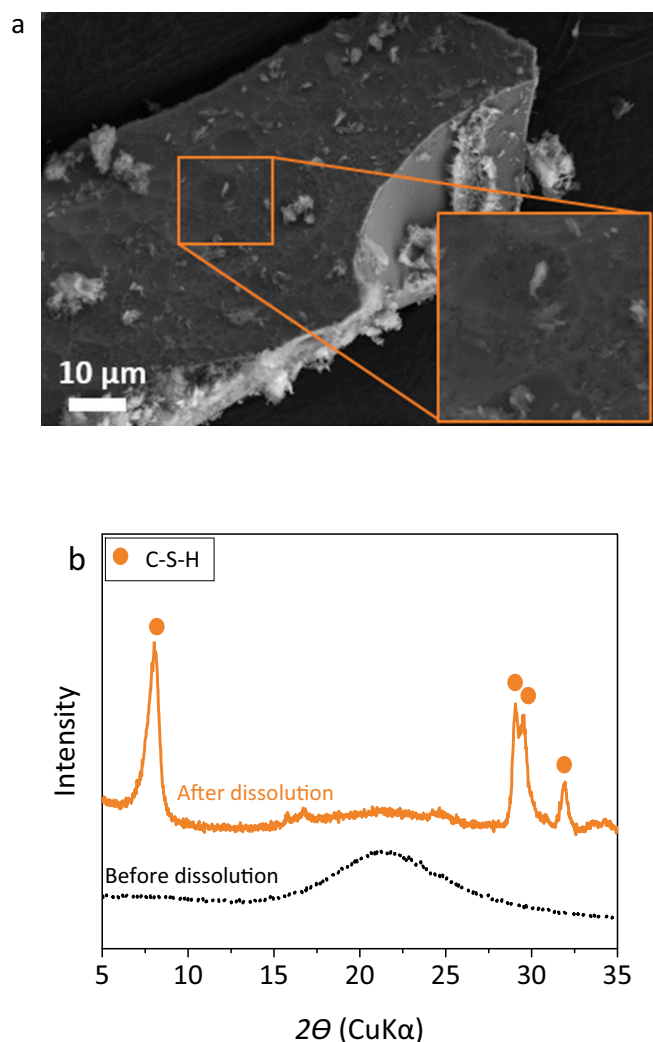


Fig. 9. a) SEM secondary electron images and b) XRD of amorphous silica before and after 12 months of dissolution (AmS-1: amorphous  $\text{SiO}_2$  plus C-S-H) at 40 °C.

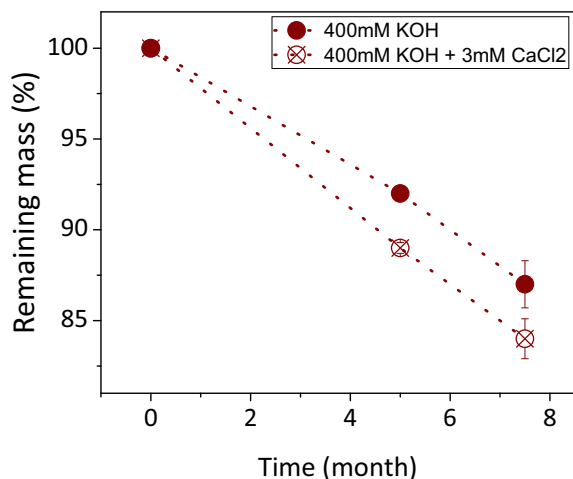


Fig. 10. Decrease of mass (%) of AmS-PI in 400 mM KOH without and with 3 mM  $\text{CaCl}_2$  at 60 °C as a function of time. The error bars show the standard deviation of the values.

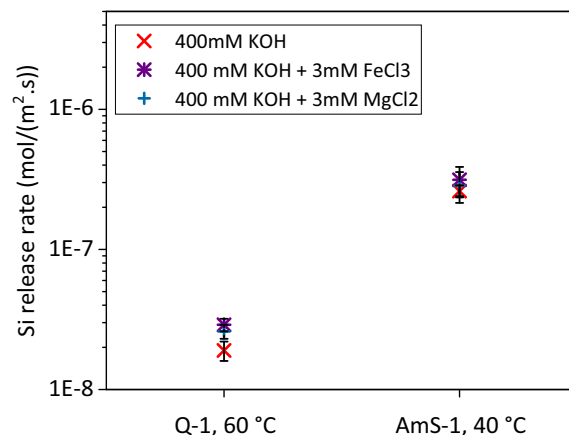


Fig. 11. The Si release rate ( $\text{mol}/(\text{m}^2\cdot\text{s})$ ) from a) Q-1 at 60 °C and b) AmS-1 at 40 °C in 400 mM KOH, 400 mM KOH + 3 mM  $\text{FeCl}_3$  and 400 mM KOH + 3 mM  $\text{MgCl}_2$ . All error bars were calculated with respect to 95% confidence interval.

shows some of the experimental measurements. The results indicate also that the presence of C-S-H did not prevent the dissolution of amorphous silica, in contrast to previous reports [26,27].

Some studies have suggested, based on measurements of mass loss [26,27] or silicon concentrations [28], that Ca slows down the dissolution of silica due to the formation of a protective C-S-H layer on its surface. However, the study of mass losses and silicon concentrations in the presence of precipitating C-S-H contradicts this hypothesis. The formation of C-S-H did not create a protective layer as the silica surface keeps reacting, as visible in the SEM image (Fig. 9a), and the continuing mass loss (Fig. 10). The formation of new solids during dissolution experiments means that dissolution rates cannot be measured from the development of silicon concentrations or weighing results, as both dissolution and precipitation are occurring at the same time.

In agreement with the observations reported here, an acceleration of quartz dissolution has been reported in the presence of  $\text{Ca}^{2+}$  at near neutral pH conditions, although the effect was more moderate than observed here [15,16]. Dove has related the accelerating effect of different bivalent cations,  $\text{M}^{2+}$ , with their ability to form surface complexes  $\equiv\text{Si}-\text{O}-\text{M}^+$  which lower the strength of the  $\equiv\text{Si}-\text{O}-\text{Si}\equiv$  bonds and follow the size of the ion radius:  $\text{Ba}^{2+} > \text{Sr}^{2+} > \text{Ca}^{2+} > \text{Mg}^{2+}$ . Based on their sequence (which also agrees with the sequences of earth alkali ions

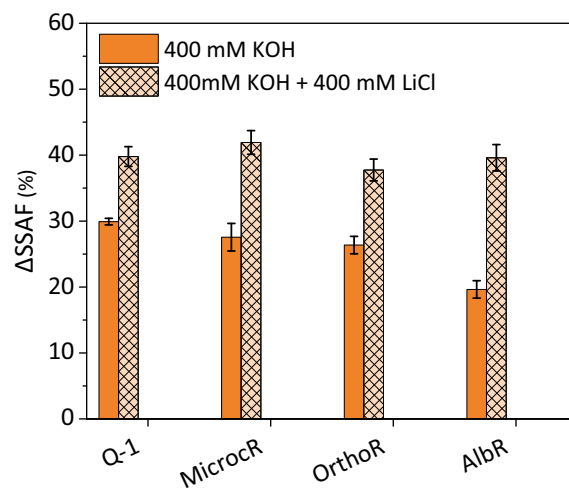
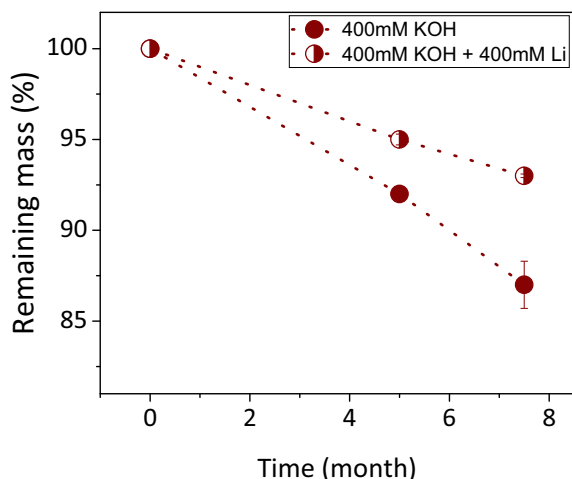


Fig. 12. The change of the scratch surface area of quartz ( $\Delta\text{SSAF}$ , %) (Q-1), microcline (MicrocR), orthoclase (OrthoR) and albite (AlbR) after 21 days of dissolution in 400 mM KOH and in 400 mM KOH + 400 mM  $\text{LiCl}$  at 40 °C. The error bars show the standard deviation of the values.



**Fig. 13.** Decrease of mass of AmS-PI in 400 mM KOH without and with 400 mM LiCl at 60 °C as a function of time. The error bars show the standard deviation of the values.

for sorption on C-S-H [56]), an even stronger accelerating effect of  $\text{Sr}^{2+}$ ,  $\text{Ba}^{2+}$  or  $\text{Ca}^{2+}$  on  $\text{SiO}_2$  dissolution at high pH values can be expected.

### 3.4. Effect of Fe and Mg

The presence of 3 mM Mg or Fe(III) in the starting solution did not significantly affect the dissolution rate of quartz or amorphous silica in 400 mM KOH as shown in Fig. 11. This could rather be related to the very low solubility of brucite,  $\text{Mg}(\text{OH})_2$ , and hematite (or other iron hydroxides) at high pH resulting in expected Mg and Fe(III) concentrations of below 0.001 mM at pH 13 (Fig. E1). The very low concentrations of Mg and Fe could thus explain why no effect on the dissolution rate was observed in the high pH conditions studied here.

In contrast, Dove [15,16] reported at near neutral pH conditions and at higher Mg concentrations, a slower dissolution of quartz in the presence of  $\text{Mg}^{2+}$  than in the presence of  $\text{Ca}^{2+}$  or of alkali ions, which was assigned to a lower tendency of  $\text{Mg}^{2+}$  to form surface complexes as discussed above. For iron an inhibiting effect could be expected [5,15], indicating that both Mg and Fe could potentially slow down dissolution.

### 3.5. Effect of Li on dissolution rate of silica and feldspars

#### 3.5.1. Dissolution by scratch tracking

The scratch-tracking technique indicated that the presence of 400 mM LiCl increased the dissolution rate of quartz, microcline, orthoclase and albite clearly as shown in Fig. 12.

#### 3.5.2. Dissolution in diluted solution and based on mass loss

Li increased the release rate of Si from albite and microcline, while for amorphous silica and quartz slower Si release rates were measured (Table 3). The lower silicon concentrations observed in the presence of Li for amorphous silica and quartz could be due to the formation of  $\text{Li}_2\text{SiO}_3$  (as discussed below and as reported by [27]), which limits the Si concentrations in solution.

Fig. 13 shows the decrease of mass (%) of a silica plate in 400 mM KOH without and with 400 mM LiCl. The remaining mass (%) of AmS-PI was higher in the presence of Li, in agreement with the dissolution results but in contrast with SEM observations. The formation of  $\text{Li}_2\text{SiO}_3$  was detected by XRD after 5 months of reaction in 400 mM + 400 mM LiCl (Fig. G1), which would explain the apparently increased mass of

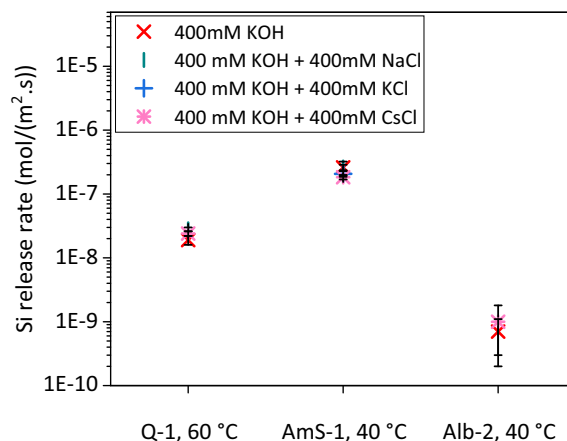


**Fig. 14.** The Si release rate ( $\text{mol}/(\text{m}^2\cdot\text{s})$ ) from Q-1 (at 60 °C) and AmS-1 and Alb-2 (at 40 °C) in 400 mM KOH, 400 mM KOH and 400 mM of NaCl or KCl or CsCl. All error bars were calculated with respect to 95% confidence interval.

these samples, in agreement with the previous results of  $\text{SiO}_2$  dissolution in the presence of lithium [27].

By the scratch-tracking method, increased dissolution of silica and feldspars was observed in the presence of Li; while the dissolution, as well as the mass loss experiments, showed an apparent slower dissolution, which seems to be related to the precipitation of  $\text{Li}_2\text{SiO}_3$  or similar Li-Si-oxides, which decreased the aqueous Si concentrations and increased the mass of the solid. The scratch-tracking method and observation of the solid surfaces showed directly that lithium can accelerate the dissolution of Si-containing solids at high pH values. It should be noted that at near neutral pH a small reduction of silica dissolution [34] or no significant effect was observed [15,16], indicating that the pH could play an important role in the effect of Li on dissolution. Based on the observations of Dove [16], the ability of  $\text{Li}^+$  to form surface complexes on silica could be responsible for its accelerating effect on  $\text{SiO}_2$  dissolution.

Based on the findings discussed above, lithium rather accelerates the dissolution of silica and feldspars, and thus, it is expected to increase the dissolution rate of silica-rich aggregates. However the presence of both

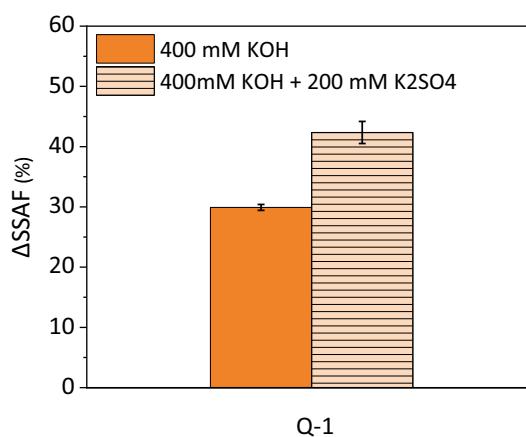


**Fig. 15.** The change of the scratch surface area of quartz ( $\Delta\text{SSAF}$ , %) (Q-1) after 21 days of dissolution in 400 mM KOH and 400 mM KOH + 200 mM  $\text{K}_2\text{SO}_4$  at 40 °C. The error bars show the standard deviation of the values.

Ca and Li might slow down silica dissolution [18]. The role of lithium to prevent ASR expansion is not necessarily because of a slow down of the dissolution rate, but rather due to the formation of a different ASR product. The presence of lithium is reported to lead to an ASR product containing Li but with lower  $\text{CaO/SiO}_2$  and  $(\text{Na} + \text{K})/\text{Si}$  [31,32].

### 3.6. Effect of Na, K and Cs

Fig. 14 shows that the presence of additional 400 mM of NaCl or KCl or CsCl had no significant effect on the dissolution rates of quartz, amorphous silica or albite, although the values measured in the presence of Cs tended to be slightly lower. This is in agreement with the observation of Dove [15,16] at near neutral pH conditions, where only a small difference between the different alkali ions on the dissolution kinetics of  $\text{SiO}_2$  was observed. Interestingly at near neutral pH values also Li shows no or only a very moderate accelerating effect [15,16], in contrast to the high pH conditions studied here, where Li shows a clearly accelerating effect resulting in the following sequence:  $\text{Li}^+ \gg \text{Na}^+ \approx \text{K}^+ \approx (>) \text{Cs}^+$ , which follow their tendency to form surface complexes with  $\text{SiO}_2$  as detailed in [15,16].

### 3.7. Effect of sulfate

The scratch-tracking method showed that the addition of 200 mM of  $\text{K}_2\text{SO}_4$  to 400 mM KOH moderately increased quartz dissolution (Fig. 15). In contrast, the dissolution studies showed no significant effect of  $\text{K}_2\text{SO}_4$  on the dissolution rate of amorphous silica (Table 3). The presence of 50 mM  $\text{K}_2\text{SO}_4$  did not change the dissolution rate of amorphous silica (AmS-1) samples exposed to 400 mM KOH + 3 mM  $\text{AlCl}_3$  (Table 3). The increased dissolution by the scratch tracking method agrees with observations at neutral pH, where an increase of silica dissolution was observed in the presence of sodium sulfate [57]. The acceleration of the dissolution rate was related to the specific adsorption of  $\text{SO}_4^{2-}$  ions on the surface of amorphous silica, resulting in a decrease in the strength of the  $\equiv\text{Si}-\text{O}-\text{Si}\equiv$  bonds [57]. Whether specific adsorption of sulfate on  $\text{SiO}_2$  also occurs at high pH values or whether other effects are responsible for the observed increase of dissolution remains presently unclear as well as why different results were observed by the two different methods.

## 4. Conclusions

The comparison of different methods (increase of scratch width, measurement of the increase of Si concentrations, and measurement of mass changes) indicated that the measurement of Si concentrations as well as the mass changes were strongly affected by the formation of secondary phases such as C-S-H and lithium silicates, which led to misleading results. The direct observation of the increase of the scratched area was shown to be the most reliable method in the presence of Ca and Li, where secondary solids formed, while consistent trends were observed in the absence of secondary phases.

All three methods can be used to study dissolution. However, while the dissolution method allows quantifying the dissolution rate, the scratch tracking and weighing methods give only relative changes, which cannot be directly translated into dissolution rates. In the scratch-tracking method, only a one-dimensional change (widening of the scratches) is measured during relatively short periods of time (up to 21

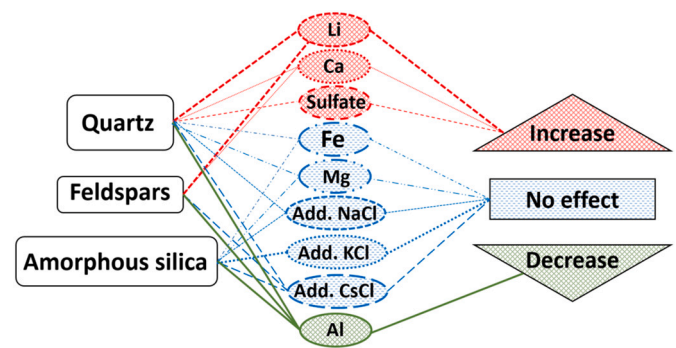


Fig. 16. Effect of different dissolved ions on the dissolution rate of amorphous silica, quartz and feldspars under alkaline conditions.

days), while the 3-dimensional reactions up to 1 year and 7.5 months are captured by the dissolution and weighing method, respectively. And as shown here, both the dissolution and weighing method can be affected by the simultaneous occurrence of dissolution and precipitation, which makes interpretation of the results impossible. Thus a combination of at least two of the methods and a careful investigation of the samples after analysis seems most promising to get reliable results.

The results show that:

- o The dissolution rate of silica, quartz and feldspar increased as expected with the surface area, pH values and temperature.
- o Among all studied ions, only Al could effectively slow down the dissolution of quartz, amorphous silica, Na-feldspar and K-feldspar as illustrated in Fig. 16. The slowdown was more distinct at pH 12.5 than at pH 13, which could be associated with a higher tendency of Al to sorb on the surface at lower pH values. The most efficient way to increase Al concentrations in the pore solutions of cement pastes (without increasing the pH value) is the use of Al-rich SCMs such as fly ash or metakaolin, which increases the Al-concentration in the pore solution [36,58,59], and which have been observed to contribute significantly to reduce ASR expansion.
- o The presence of Ca accelerated the dissolution of  $\text{SiO}_2$  and feldspars, indicating that Ca is not only used to form ASR products [60] but that its presence further accelerates the dissolution. As the calcium concentrations are strongly influenced by pH value, higher calcium concentrations are present at lower pH values in PC, while the presence of Si-rich SCMs [11] has relatively little influence on the measured calcium concentrations as at the same time pH decreases. Therefore, it is rather the decrease of pH values in the pore solution of blended cement pastes with Si-rich SCMs than lower Ca concentrations that are expected to be the reason for the slower ASR expansion in the presence of SCMs [11,61].
- o The presence of Fe and Mg had no significant effect on the dissolution rate, which was assigned to the very low solubility of iron hydroxide and brucite at pH 12.5 to 13.
- o The presence of additional Na, K salts in KOH solutions did not affect the dissolution rate, while Cs showed a very weak suppression and Li showed a clear acceleration. This might be related to the higher tendency of Li to form surface complexes [15,16] resulting in the following sequence of dissolution rates:  $\text{Li}^+ \gg \text{Na}^+ \approx \text{K}^+ \approx (>) \text{Cs}$ . Thus, the suppression or slow down of ASR in the presence of Li is not

related to its effect on silica dissolution kinetics but rather to the formation of a different ASR product [31,32].

- o The presence of sulfate seems also to slightly increase the dissolution of  $\text{SiO}_2$ , although the results are not that clear. Both the effect of sulfate as well as the possible interplay between sulfate and calcium on the dissolution of  $\text{SiO}_2$  could be further investigated.

The dissolution experiments, conducted here, allowed the study of the effect of different parameters separately. In the pore solution of cement pastes, however, many different elements are present simultaneously and their concentrations depend on pH values. The present studies underline the importance of alkali hydroxide concentrations and thus pH values, not only for the formation of ASR products but also for the dissolution kinetics of silica-containing minerals present within the aggregates [5]. This is in good agreement with the faster expansion due to ASR formation observed at high pH values [2,21,61,62].

#### CRedit authorship contribution statement

**M. Bagheri:** Methodology, Formal analysis, Investigation, Measurement, Modelling, Writing – Original Draft, Visualization.

**B. Lothenbach:** Methodology, Formal analysis, Validation, Resources, Modelling, Writing – Review & Editing, Supervision, Funding acquisition.

**M. Shakoorioskooie:** Image processing, Writing & Editing.

**K. Scrivener:** Methodology, Validation, Review & Editing, Supervision, Funding acquisition.

#### Declaration of competing interest

The authors declare that they have no known competing financial interests or personal relationships that could have appeared to influence the work reported in this paper.

#### Acknowledgments

The authors acknowledge the SNF Sinergia project: Alkali-silica reaction in concrete (ASR), grant number CRSII5\_17108 for support of M. Bagheri and M. Shakoorioskooie. We would like to thank Dr. Andreas Jenni, the University of Berne for providing the natural feldspars and Luigi Brunetti (Empa) for the IC measurements.

#### Appendix A. Surface area of the segmented scratches

A summary of the method used to quantify the increase of scratch width after exposure as detailed in [39] is added for the convenience of the reader. After segmenting (by using a threshold to the pixel values) of the scratches in an SEM image (inset (a) of the figure below), a new image is produced which is called the binary image of the segmented scratches. An example of the binary image is shown in the inset (b) of the figure below. The word “binary” for such images indicates that they have solely two features, a foreground and a background. In other words, all of the pixels in such images could be classified into two groups (foreground and background), each associated with a single pixel value. For instance, in the inset (b) of the figure below, the segmented scratches (yellow) are foreground and all of their pixel values are 1. Whereas, the black space surrounding them is considered background with the pixel value of 0.

Computing the surface area of the segmented scratches is conducted by counting the total number of the foreground square pixels in these images. Then this value is multiplied by the actual pixel size of the corresponding SEM image (considering the scale bar the pixel size could be determined) to obtain the physical surface area of the segmented scratches.

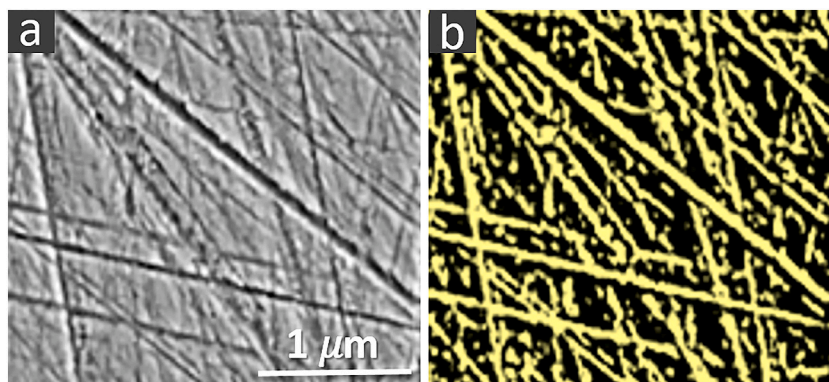


**Fig. A1.** Example images for the scratches observed in the SEM images and the corresponding segmented scratches (a) the small region of interest from SEM image acquired from Fig. 6(b), and b) the segmented scratches (binary scratches).

##### A.1. Specific surface area

One to two g of the powder (randomly sampled from a larger well-mixed batch) was mixed with epoxy resin and placed in silicon mold. After 1 day, the impregnated powder was polished to 1  $\mu\text{m}$  using hard disc and diamond spray. Backscattered-SEM image mapping was carried out on the surfaces



of polished (and coated with carbon) specimens, each image having a pixel size of  $2.44 \times 2.44 \mu\text{m}^2$ . The collected images (24 SEM images,  $6 \times 4$ ) were stitched together using Fiji software to form a single image (Fig. A2(a)). Each individual SEM image (used in the stitched map) was acquired with a magnification of  $100\times$ , with a resolution of 1024 pixels, electron beam voltage of 15 kV and a working distance of 11 mm.

The specific surface area of the powders was estimated based on the 2-dimensional (2D) cross-sections observed in these large stitched SEM images (Fig. A2). At least three SEM images for each type of mineral powder were used for the specific surface area estimation. In the SEM images, the powder particles were first segmented. To do so, pixel-value thresholding was implemented on the SEM images, resulting in a new binary image of the particles (differentiating the powder particles as foreground with a constant assigned value of one to their pixels and the one of epoxy resin as background with a constant assigned value of zero to their pixels). Then the particles in the binary images were labelled and each of them was associated with a random color (to demonstrate the independence of each particle), as illustrated in Fig. A2(b). Then shape tensor analysis was carried out to determine the 2D bounding box extents (“a” and “b” values shown in Fig. A3(a)) of each individual object (powder particle) in the binary image based on their Eigenvectors/values [63].

In order to approximate a 3-dimensional (3D) powder particle based on its 2D binary mask, the extent for the third dimension (“c” or Extent 3 =  $2\epsilon_3\lambda_3$ ) was computed as the average of its “a” and “b” values (Fig. A3(b)). The smooth surface area of an equivalent ellipsoid with the dimensions of  $a > c > b$  for each particle was computed (Fig. A3(c)). The volume of each ellipsoid was also calculated to estimate the approximate mass of each particle using the density of the corresponding mineral being analyzed. Finally, the specific surface area was estimated by dividing the surface area of the equivalent ellipsoid by the approximate mass of each particle (with a unit of  $\text{m}^2/\text{kg}$ ).

The relatively large standard deviation for some of the estimated specific surface area values originates from the extremely non-homogeneous particle size distributions. In cases where the powder sizes distribution is quite narrow, the standard deviation also reduces.

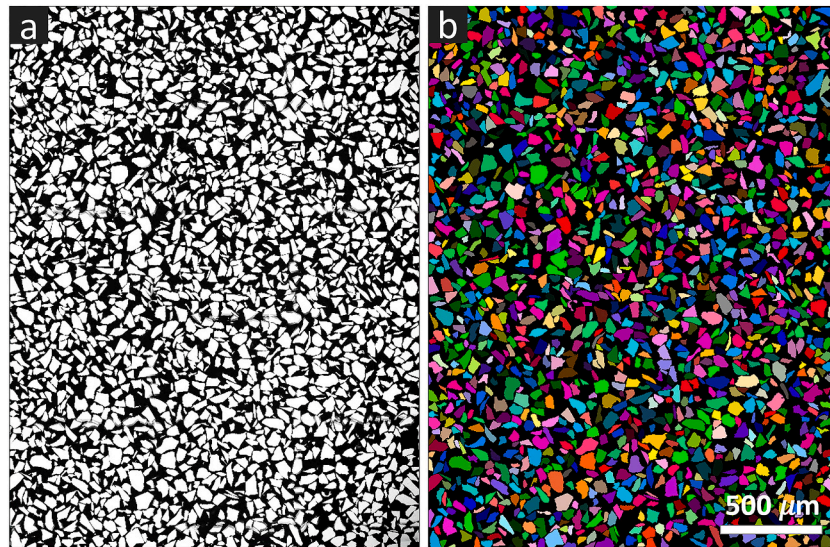


Fig. A2. (a) An example SEM image for amorphous silica mineral illustrating the 2D cross-section of powder particles (the micrograph was obtained by stitching several SEM images) and (b) the labelled binary particles after shape tensor analysis, each associated with a random color to demonstrate the independence of each particle.

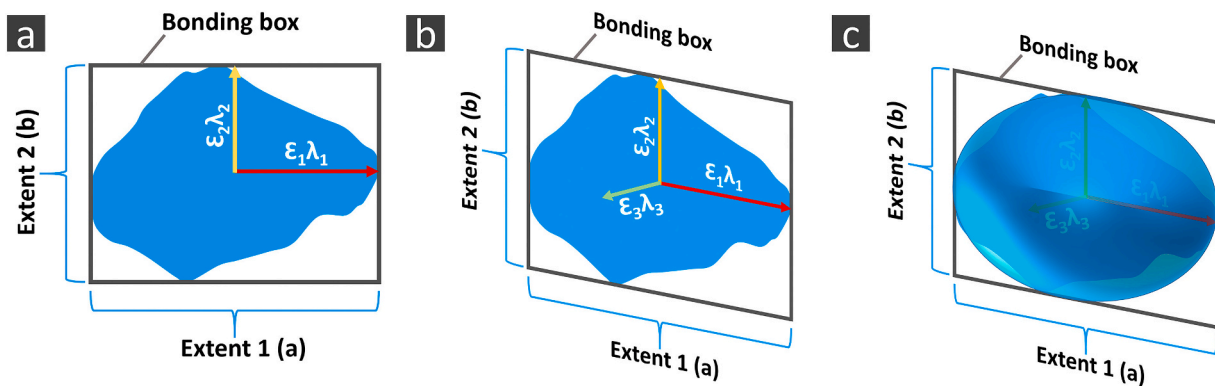
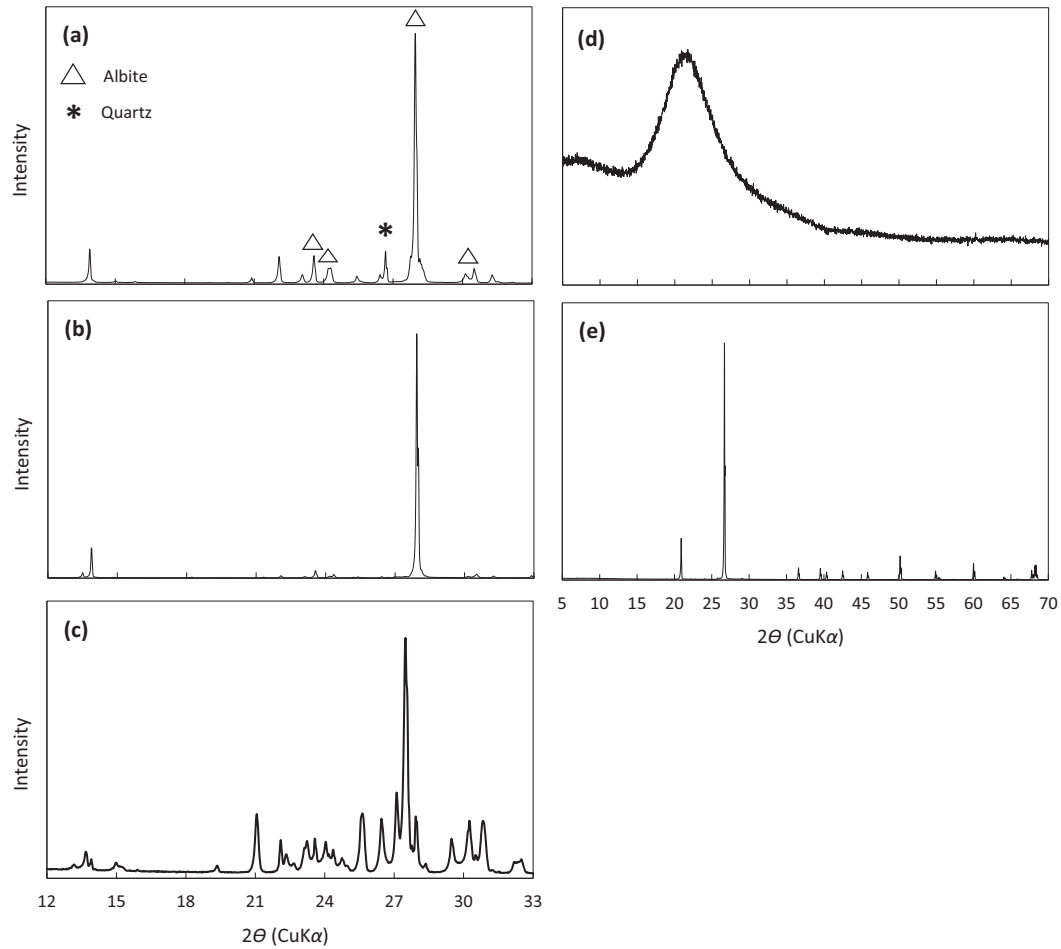


Fig. A3. Schematic illustration of the results of shape tensor analysis on a binary mask of an individual particle: (a) 2D cross-section of a particle with shape tensor components, (b) approximated third dimension extent and (c) equivalent ellipsoid passing with dimensions of three extent values computed for the particle.



## Appendix B. Sample characterization



**Fig. B1.** XRD patterns of a) albite (Alb-1), b) albite (AlbS/Alb-2), c) microcline (MicrocR/Microc), d) amorphous silica (AmS-1/2) and e) quartz (Q-1/2) powder before the dissolution experiments.

## Appendix C. Saturation indices

**Table C1**

The measured and estimated concentrations used to calculate saturation indices using GEMS.

Solid/solution	Time (month)	Si (mmol/l)	Ca <sup>a</sup> (mmol/l)	Al <sup>b</sup> (mmol/l)
AmS-1 400 mM KOH	1	2.6	0	0
	2.3	4.2		
	3.3	6.6		
	5.8	10.4		
	8.8	14.85		
AmS-1 400 mM KOH + 3 mM CaCl <sub>2</sub>	1	0.2	3	0
	2.3	1.3		
	3.3	0.8		
	5.8	4.3		
	8.8	8.33		
Q-2 400 mM KOH	1	0.18	0	0
	2.3	1.4		
	3.3	0.7		
	5.8	1.2		
	8.8	1.95		
	12	2.3		
	14	2.7		
	16	3.1		
Alb-1 400 mM KOH	18	3.5	0	0.09
	0.9	0.28		
	1.9	0.33		
	3	0.22		
	5.2	0.45		
	7.5	0.6		

(continued on next page)

**Table C1** (continued)

Solid/solution	Time (month)	Si (mmol/l)	Ca <sup>a</sup> (mmol/l)	Al <sup>b</sup> (mmol/l)
Microc 400 mM KOH	9.3	0.61	0	0.2
	11.6	0.88		0.29
	14.2	0.87		0.29
	8	0.13		0.04
	11	0.12		0.04
	12	0.19		0.06

<sup>a</sup> The initial concentration of added CaCl<sub>2</sub> was considered, as all measurements were below the detection limit.

<sup>b</sup> The expected concentration of Al was considered; Al (mmol/L) = 1/3 of released Si (mmol/L), as all measurements were below the detection limit.

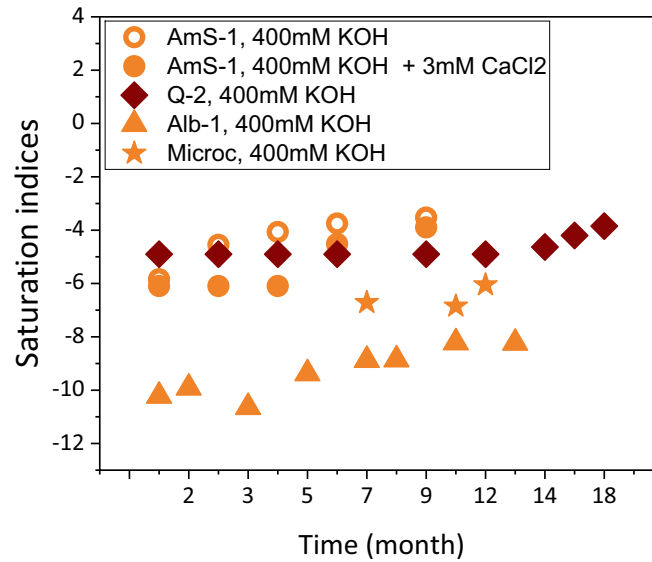


**Fig. C1.** Saturation indices calculated using GEMS based on the data shown in Table C1, with respect to amorphous silica (AmS-1), quartz (Q-1), albite (Alb-1) and microcline (Microc) in 400 mM KOH, as a function of time. Storage temperatures: orange symbol at 40 °C and dark red symbols at 60 °C. (For interpretation of the references to color in this figure legend, the reader is referred to the web version of this article.)

## Appendix D

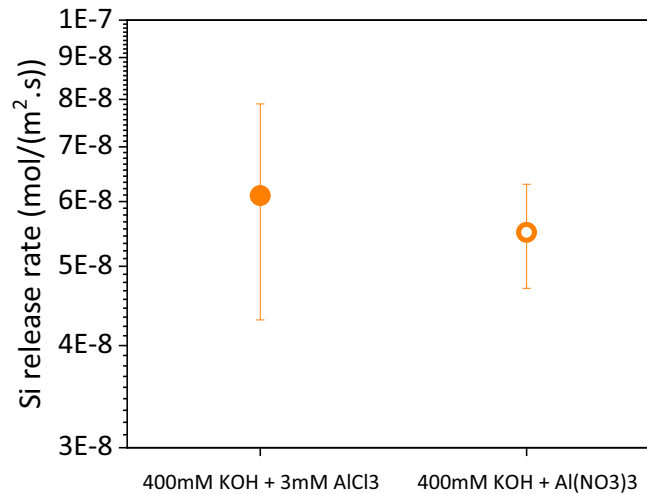


**Fig. D1.** The effect of counter anions on the dissolution rate of amorphous silica in 400 mM KOH + 3 mM of Al, provided by the addition of AlCl<sub>3</sub> or Al(NO<sub>3</sub>)<sub>3</sub>·9H<sub>2</sub>O at 40 °C. All error bars were calculated with respect to a 95% confidence interval.

## Appendix E. Solubility and Al speciation

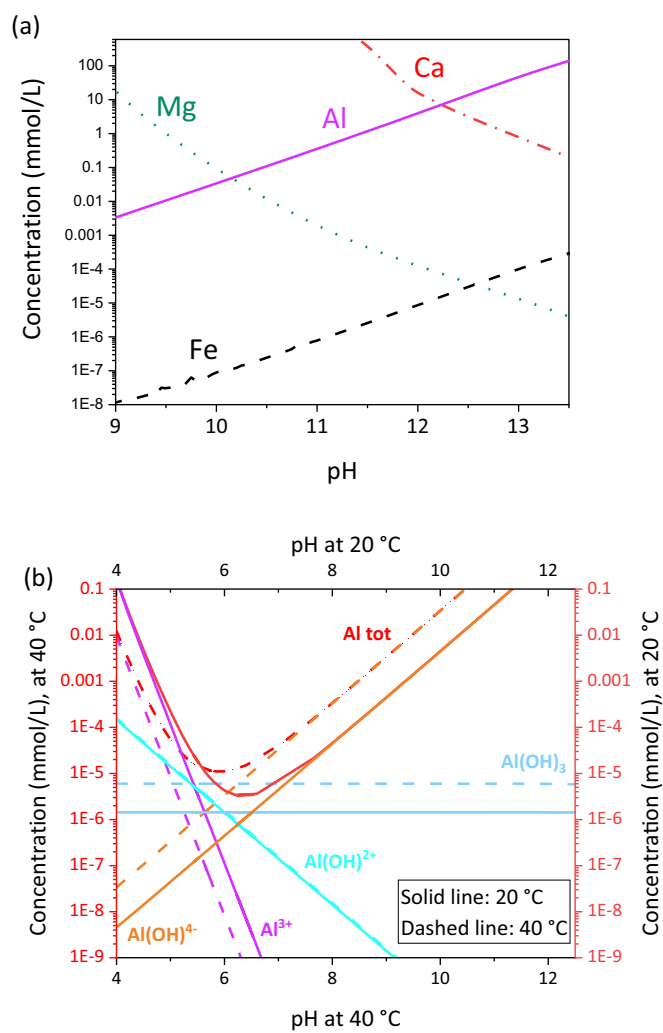


**Fig. E1.** The solubility of a) gibbsite, portlandite, brucite and hematite in (mmol/L) at 40 °C and b) microcrystalline  $\text{Al}(\text{OH})_3$  and its specimens (mmol/L) as a function of pH at 20 and 40 °C, calculated by GEMS.

## Appendix F. Scratch tracking

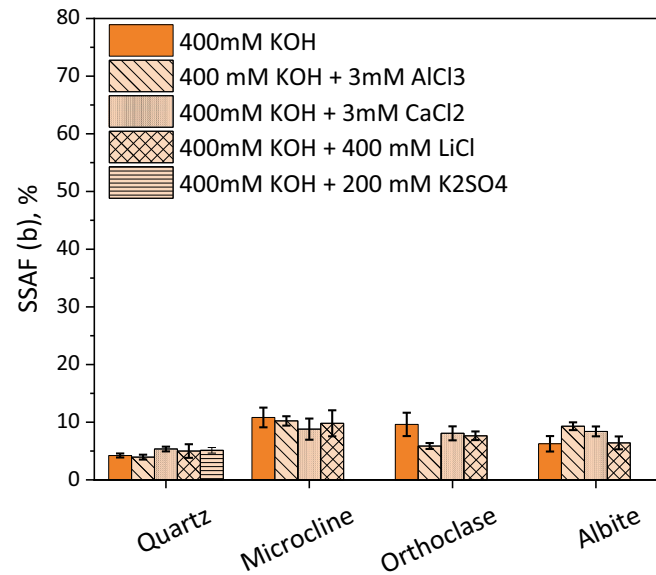


**Fig. F1.** Scratched surface area fraction (SSAF, %) of quartz (Q-1), microcline (MicroR), orthoclase (OrthoR) and albite (AlbR) before exposure to different solutions (400 mM KOH, 400 mM KOH + 3 mM AlCl<sub>3</sub>, 400 mM KOH + 3 mM CaCl<sub>2</sub>, 400 mM KOH + 400 mM LiCl and 400 mM KOH + 200 mM K<sub>2</sub>SO<sub>4</sub>). The error bars show the standard deviation of the values.

**Table F1**

The change of the scratched surface area fraction of quartz (Q-1) before and after exposure to different solutions.

Solution	Time (day)	SSAF (%)				ΔSSAF (%)				Average ΔSSAF (%)	Standard deviation
		Area 1	Area 2	Area 3	Area 4	Area 1	Area 2	Area 3	Area 4		
400 mM KOH	0	4.6	4.4	4.1	3.8	30.3	29.3	30.3	29.8	29.9	0.5
	21	34.9	33.7	34.4	33.6						
400 mM KOH + 3 mM AlCl <sub>3</sub>	0	4.5	3.8	4.0	3.5	19.6	23.8	22.9	21.5	22.0	1.8
	21	24.1	27.6	26.9	25						
400 mM KOH + 3 mM CaCl <sub>2</sub>	0	5.6	4.8	5.7	5.3	36.0	37.2	34.3	36.3	36.0	1.2
	21	41.6	42.0	40.1	41.6						
400 mM KOH + 400 mM LiCl	0	5.3	4.4	3.8	6.5	39.5	39.7	41.8	38.2	40.0	1.5
	21	44.8	44.1	45.6	44.7						
400 mM KOH + 200 mM K <sub>2</sub> SO <sub>4</sub>	0	4.5	5.5	5.0	5.5	42.5	44.4	42.6	40.0	42.4	1.8
	21	47	50.0	48.0	45.5						

## Appendix G. Characterization of formed solids during dissolution

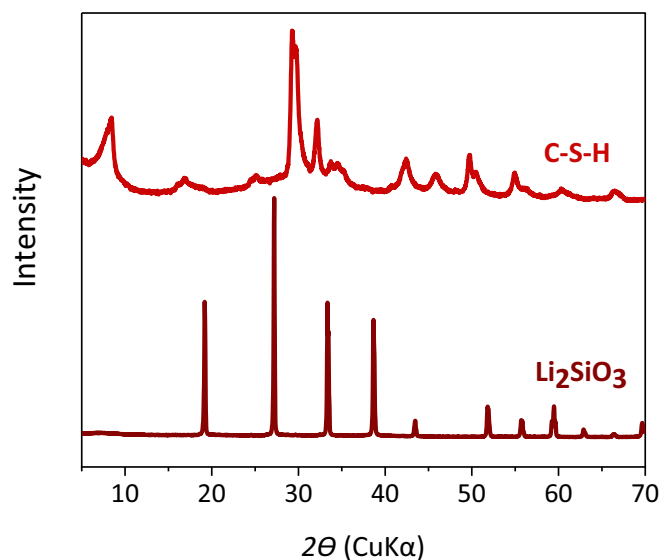


**Fig. G1.** XRD patterns of C-S-H and  $\text{Li}_2\text{SiO}_3$  which formed due to dissolution of amorphous silica plates (AmS-Pl) in 400 mM KOH + 3 mM  $\text{CaCl}_2$  and 400 mM KOH + 400 mM LiCl respectively at 60 °C after 5 months.

**Table G1**

Mass change of AmS-Pl in 400 mM KOH without and with 3 mM  $\text{CaCl}_2$  at 60 °C as a function of time.

Solution	Mass (g)	
	Before dissolution	After 7.5 months of dissolution
400 mM KOH	2.240	1.963
	2.241	1.929
400 mM KOH + 3 mM $\text{CaCl}_2$	2.176	1.83
	2.174	1.816
400 mM KOH + 400 mM LiCl	2.235	2.066
	2.244	2.078

## References

- [1] L. Valentini, M. Favero, M.C. Dalconi, V. Russo, G. Ferrari, G. Artioli, Kinetic model of calcium-silicate hydrate nucleation and growth in the presence of PCE superplasticizers, *Cryst. Growth Des.* 16 (2016) 646–654, <https://doi.org/10.1021/acs.cgd.5b01127>.
- [2] T. Chappex, K. Scrivener, Alkali fixation of C-S-H in blended cement pastes and its relation to alkali silica reaction, *Cem. Concr. Res.* 42 (2012) 1049–1054, <https://doi.org/10.1016/j.cemconres.2012.03.010>.
- [3] L.S. Dent Glasser, N. Kataoka, The chemistry of “alkali-aggregate” reaction, *Cem. Concr. Res.* 11 (1981) 1–9.
- [4] A. Leemann, L. Holzer, Alkali-aggregate reaction-identifying reactive silicates in complex aggregates by ESEM observation of dissolution features, *Cem. Concr. Compos.* 27 (2005) 796–801, <https://doi.org/10.1016/j.cemconcomp.2005.03.007>.
- [5] S.L. Brantley, A.F. White, J.D. Kubicki, *Kinetics of Water-Rock Interaction*, Springer Science + Business Media, New York, 2008, <https://doi.org/10.1007/978-0-387-73563-4>.
- [6] G. Yuan, Y. Cao, H.-M. Schulz, F. Hao, J. Gluyas, K. Liu, T. Yang, Y. Wang, K. Xi, F. Lia, A review of feldspar alteration and its geological significance in sedimentary basins: from shallow aquifers to deep hydrocarbon reservoirs, *Earth Sci. Rev.* 191 (2019) 114–140, <https://doi.org/10.1016/j.earscirev.2019.02.004>.
- [7] C. Drolet, J. Duchesne, B. Fournier, Effect of alkali release by aggregates on alkali-silica reaction, *Constr. Build. Mater.* 157 (2017) 263–276, <https://doi.org/10.1016/j.conbuildmat.2017.09.085>.
- [8] P.M. Dove, N. Han, A.F. Wallace, J.J. De Yoreo, Kinetics of amorphous silica dissolution and the paradox of the silica polymorphs, *Proc. Natl. Acad. Sci.* 105 (2008) 9903–9908, <https://doi.org/10.1073/pnas.0803798105>.
- [9] P.M. Dove, The dissolution kinetics of quartz in sodium chloride solutions at 25° to 300°C, *Am. J. Sci.* 294 (1994) 665–712, <https://doi.org/10.2475/ajs.294.6.665>.
- [10] J.P. Icenhower, P.M. Dove, The dissolution kinetics of amorphous silica into sodium chloride solutions: effects of temperature and ionic strength, *Geochim. Cosmochim. Acta* 64 (2000) 4193–4203, [https://doi.org/10.1016/S0016-7037\(00\)00487-7](https://doi.org/10.1016/S0016-7037(00)00487-7).
- [11] A. Vollpracht, B. Lothenbach, R. Snellings, J. Haufe, The pore solution of blended cements: a review, *Mater. Struct. Constr.* 49 (2016) 3341–3367, <https://doi.org/10.1617/s11527-015-0724-1>.
- [12] F. Rajabipour, E. Giannini, C. Dunant, J.H. Ideker, M.D.A. Thomas, Alkali-silica reaction: current understanding of the reaction mechanisms and the knowledge gaps, *Cem. Concr. Res.* 76 (2015) 130–146, <https://doi.org/10.1016/j.cemconres.2015.05.024>.
- [13] B.R. Bickmore, K.L. Nagy, A.K. Gray, A.R. Brinkerhoff, The effect of  $\text{Al}(\text{OH})_4^-$  on the dissolution rate of quartz, *Geochim. Cosmochim. Acta* 70 (2006) 290–305, <https://doi.org/10.1016/j.gca.2005.09.017>.
- [14] T. Chappex, K.L. Scrivener, The influence of aluminium on the dissolution of amorphous silica and its relation to alkali silica reaction, *Cem. Concr. Res.* 42 (2012) 1645–1649, <https://doi.org/10.1016/j.cemconres.2012.09.009>.
- [15] P.M. Dove, The dissolution kinetics of quartz in aqueous mixed cation solutions, *Geochim. Cosmochim. Acta* 63 (1999) 3715–3727, [https://doi.org/10.1016/S0016-7037\(99\)00218-5](https://doi.org/10.1016/S0016-7037(99)00218-5).
- [16] P.M. Dove, C.J. Nix, The influence of the alkaline earth cations, magnesium, calcium, and barium on the dissolution kinetics of quartz, *Geochim. Cosmochim. Acta* 61 (1997) 3329–3340, [https://doi.org/10.1016/S0016-7037\(97\)00217-2](https://doi.org/10.1016/S0016-7037(97)00217-2).
- [17] W.L. Marshall, J.M. Warakowski, Amorphous silica solubilities-II. Effect of aqueous salt solutions at 25°C, *Geochim. Cosmochim. Acta* 44 (1980) 915–917, [https://doi.org/10.1016/0016-7037\(80\)90281-1](https://doi.org/10.1016/0016-7037(80)90281-1), 919–924.
- [18] A. Leemann, L. Lörtscher, L. Bernard, G. Le Saout, B. Lothenbach, R.M. Espinosa-Marzal, Mitigation of ASR by the use of  $\text{LiNO}_3$  - characterization of the reaction products, *Cem. Concr. Res.* 59 (2014) 73–86, <https://doi.org/10.1016/j.cemconres.2014.02.003>.
- [19] A. Leemann, L. Bernard, S. Alahache, F. Winnefeld, ASR prevention — effect of aluminium and lithium ions on the reaction products, *Cem. Concr. Res.* 76 (2015) 192–201, <https://doi.org/10.1016/j.cemconres.2015.06.002>.
- [20] J. Zhou, K. Zheng, Z. Liu, L. Chen, N. Lippiatt, Use of  $\gamma\text{-Al}_2\text{O}_3$  to prevent alkali-silica reaction by altering solid and aqueous compositions of hydrated cement



- paste, *Cem. Concr. Res.* 124 (2019) 1–8, <https://doi.org/10.1016/j.cemconres.2019.105817>.
- [21] M.J. Tapas, L. Sofia, K. Vessalas, P. Thomas, V. Sirivivatnanon, K. Scrivener, Efficacy of SCMs to mitigate ASR in systems with higher alkali contents assessed by pore solution method, *Cem. Concr. Res.* 142 (2021) 1–11, <https://doi.org/10.1016/j.cemconres.2021.106353>.
- [22] T. Chappex, K.L. Scrivener, The effect of aluminum in solution on the dissolution of amorphous silica and its relation to cementitious systems, *J. Am. Ceram. Soc.* 96 (2013) 592–597, <https://doi.org/10.1111/jace.12098>.
- [23] K.J. Hüniger, The contribution of quartz and the role of aluminum for understanding the AAR with greywacke, *Cem. Concr. Res.* 37 (2007) 1193–1205, <https://doi.org/10.1016/j.cemconres.2007.05.009>.
- [24] R.K. Iler, Effect of adsorbed alumina on the solubility of amorphous silica in water, *J. Colloid Interface Sci.* 43 (1973) 399–408, [https://doi.org/10.1016/0021-9797\(73\)90386-X](https://doi.org/10.1016/0021-9797(73)90386-X).
- [25] L. Nicoleau, E. Schreiner, A. Nonat, Ion-specific effects influencing the dissolution of tricalcium silicate, *Cem. Concr. Res.* 59 (2014) 118–138, <https://doi.org/10.1016/j.cemconres.2014.02.006>.
- [26] H. Maraghechi, F. Rajabipour, C.G. Pantano, W.D. Burgos, Effect of calcium on dissolution and precipitation reactions of amorphous silica at high alkalinity, *Cem. Concr. Res.* 87 (2016) 1–13, <https://doi.org/10.1016/j.cemconres.2016.05.004>.
- [27] B. Zhou, Z. Mao, M. Deng, Reaction of quartz glass in lithium-containing alkaline solutions with or without ca, *R. Soc. Open Sci.* 5 (2018) 1–15, <https://doi.org/10.1098/rsos.180797>.
- [28] T. Oey, E.C. La Plante, G. Falzone, Y.H. Hsiao, A. Wada, L. Monfardini, M. Bauchy, J.W. Bullard, G. Sant, Calcium nitrate: a chemical admixture to inhibit aggregate dissolution and mitigate expansion caused by alkali-silica reaction, *Cem. Concr. Compos.* 110 (2020) 1–10, <https://doi.org/10.1016/j.cemconcomp.2020.103592>.
- [29] W.J. McCoy, A.G. Caldwell, New approach to inhibiting alkali-aggregate expansion, *ACI J. Proc.* 47 (1951) 693–706, <https://doi.org/10.14359/12030>.
- [30] X. Feng, M.D.A. Thomas, T.W. Bremner, B.J. Balcom, K.J. Folliard, Studies on lithium salts to mitigate ASR-induced expansion in new concrete: a critical review, *Cem. Concr. Res.* 35 (2005) 1789–1796, <https://doi.org/10.1016/j.cemconres.2004.10.013>.
- [31] X. Mo, Laboratory study of LiOH in inhibiting alkali-silica reaction at 20 °C: a contribution, *Cem. Concr. Res.* 35 (2005) 499–504, <https://doi.org/10.1016/j.cemconres.2004.06.003>.
- [32] M. Kawamura, H. Fuwa, Effects of lithium salts on ASR gel composition and expansion of mortars, *Cem. Concr. Res.* 33 (2003) 913–919, [https://doi.org/10.1016/S0008-8846\(02\)01092-X](https://doi.org/10.1016/S0008-8846(02)01092-X).
- [33] C. Tremblay, M.A. Bérubé, B. Fournier, M.D. Thomas, K.J. Folliard, Experimental investigation of the mechanisms by which LiNO<sub>3</sub> is effective against ASR, *Cem. Concr. Res.* 40 (2010) 583–597, <https://doi.org/10.1016/j.cemconres.2009.09.022>.
- [34] S. Plettinck, L. Chou, R. Wollast, Kinetics and mechanisms of dissolution of silica at room temperature and pressure, *Mineral. Mag.* 58A (1994) 728–729.
- [35] T. Oey, E. La Plante, Y.-H. Hsiao, G. Falzone, G. Sant, The role of barrier layers and reactive site deactivation on dissolution suppression: implications on mitigating alkali-silica reaction, in: 15th Int. Congr. Chem. Cem., Prague, Czech Republic, 2019.
- [36] F. Deschner, B. Lothenbach, F. Winnefeld, J. Neubauer, Effect of temperature on the hydration of Portland cement blended with siliceous fly ash, *Cem. Concr. Res.* 52 (2013) 169–181, <https://doi.org/10.1016/j.cemconres.2013.07.006>.
- [37] B. Lothenbach, F. Winnefeld, C. Alder, E. Wieland, P. Lunk, Effect of temperature on the pore solution, microstructure and hydration products of Portland cement pastes, *Cem. Concr. Res.* 37 (2007) 483–491, <https://doi.org/10.1016/j.cemconres.2006.11.016>.
- [38] B. Lothenbach, E. Bernard, U. Mäder, Zeolite formation in the presence of cement hydrates and albite, *Phys. Chem. Earth, Parts A/B/C* 99 (2017) 77–94, <https://doi.org/10.1016/j.pce.2017.02.006>.
- [39] M. Bagheri, B. Lothenbach, M. Shakoorkoskooie, A. Leemann, K. Scrivener, Use of scratch tracking method to study the dissolution of alpine aggregates subject to alkali silica reaction, *Cem. Concr. Compos.* 124 (2021) 1–11, <https://doi.org/10.1016/j.cemconcomp.2021.104260>.
- [40] R. Snellings, Solution-controlled dissolution of supplementary cementitious material glasses at pH 13: the effect of solution composition on glass dissolution rates, *J. Am. Ceram. Soc.* 96 (2013) 2467–2475, <https://doi.org/10.1111/jace.12480>.
- [41] B. Traynor, H. Uvegi, E. Olivetti, B. Lothenbach, R.J. Myers, Methodology for pH measurement in high alkali cementitious systems, *Cem. Concr. Res.* 135 (2020) 1–6, <https://doi.org/10.1016/j.cemconres.2020.106122>.
- [42] D. Midgley, A review of pH measurement at high temperatures, *Talanta* 37 (1990) 767–781, [https://doi.org/10.1016/0039-9140\(90\)80118-Y](https://doi.org/10.1016/0039-9140(90)80118-Y).
- [43] D.A. Kulik, T. Wagner, S.V. Dmytrieva, G. Kosakowski, F.F. Hingerl, K. V. Chudnenko, U.R. Berner, GEM-Selektor geochemical modeling package: revised algorithm and GEMS3K numerical kernel for coupled simulation codes, *Comput. Geosci.* 17 (2013) 1–24, <https://doi.org/10.1007/s10596-012-9310-6>.
- [44] T. Thoenen, W. Hummel, U. Berner, E. Curti, The PSI/Nagra Chemical Thermodynamic Data Base 12/07. PSI Report, 14-04, Villigen PSI, Switzerland, 2014.
- [45] B. Lothenbach, D.A. Kulik, T. Matschei, M. Balonis, L. Baquerizo, B. Dilnesa, G. D. Miron, R.J. Myers, Cemdata18: a chemical thermodynamic database for hydrated Portland cements and alkali-activated materials, *Cem. Concr. Res.* 115 (2019) 472–506, <https://doi.org/10.1016/j.cemconres.2018.04.018>.
- [46] H.C. Helgeson, J.M. Delany, H.W. Nesbitt, D.K. Bird, Summary and critique of the thermodynamic properties of rock forming minerals, *Am. J. Sci.* 278-A (1978) 1–229.
- [47] Y. Niibori, M. Kunita, O. Tochiyama, T. Chida, Dissolution rates of amorphous silica in highly alkaline solution, *J. Nucl. Sci. Technol.* 37 (2000) 349–357, <https://doi.org/10.1080/18811248.2000.9714905>.
- [48] J.M. Gautier, E.H. Oelkers, J. Schott, Are quartz dissolution rates proportional to B. E.T. Surface areas? *Geochim. Cosmochim. Acta* 65 (2001) 1059–1070, [https://doi.org/10.1016/S0016-7037\(00\)00570-6](https://doi.org/10.1016/S0016-7037(00)00570-6).
- [49] R. Wollast, L. Chou, in: A. Lerman, M. Maybeck (Eds.), *Physical and Chemical Weathering in Geochemical Cycles*, Kluwer Academic Publishers, London, 1988, <https://doi.org/10.1007/978-94-009-3071-1>.
- [50] P.V. Brady, J.V. Walther, Kinetics of quartz dissolution at low temperatures, *Chem. Geol.* 82 (1990) 253–264, [https://doi.org/10.1016/0009-2541\(90\)90084-K](https://doi.org/10.1016/0009-2541(90)90084-K).
- [51] W.A. House, D.R. Orr, Investigation of the pH dependence of the kinetics of quartz dissolution at 25°C, *J. Chem. Soc. Faraday Trans.* 88 (1992) 233–241, <https://doi.org/10.1039/FT9928800233>.
- [52] L. Chou, R. Wollast, Steady-state kinetics and dissolution mechanisms of albite, *Am. J. Sci.* 285 (1985) 963–993, <https://doi.org/10.2475/ajs.285.10.963>.
- [53] K.G. Knauss, T.J. Wolery, Dependence of albite dissolution kinetics on pH and time at 25°C and 70°C, *Geochim. Cosmochim. Acta* 50 (1986) 2481–2497, [https://doi.org/10.1016/0016-7037\(86\)90031-1](https://doi.org/10.1016/0016-7037(86)90031-1).
- [54] P.M. Dove, S.F. Elston, Dissolution kinetics of quartz in sodium chloride solutions: analysis of existing data and a rate model for 25°C, *Geochim. Cosmochim. Acta* 56 (1992) 4147–4156, [https://doi.org/10.1016/0016-7037\(92\)90257-J](https://doi.org/10.1016/0016-7037(92)90257-J).
- [55] W. Stumm, J.J. Morgan, *Aquatic Chemistry. Chemical Equilibria and Rates in Natural Waters*, 3rd ed., John Wiley & Sons, New York, 1996.
- [56] G.D. Miron, D.A. Kulik, Y. Yan, J. Tits, B. Lothenbach, Parameterization of C-S-H-(N)-(K) sublattice solid solution model for alkali uptake, *Cem. Concr. Res.* (2022). Submitted.
- [57] S. Bai, S. Urabe, Y. Okaue, T. Yokoyama, Acceleration effect of sulfate ion on the dissolution of amorphous silica, *J. Colloid Interface Sci.* 331 (2009) 551–554, <https://doi.org/10.1016/j.jcis.2008.11.076>.
- [58] F. Deschner, F. Winnefeld, B. Lothenbach, S. Seufert, P. Schwesig, S. Dittrich, F. Goetz-Neunhoffer, J. Neubauer, Hydration of Portland cement with high replacement by siliceous fly ash, *Cem. Concr. Res.* 42 (2012) 1389–1400, <https://doi.org/10.1016/j.cemconres.2012.06.009>.
- [59] F. Avet, K. Scrivener, Investigation of the calcined kaolinite content on the hydration of limestone calcined clay cement (LC3), *Cem. Concr. Res.* 107 (2018) 124–135, <https://doi.org/10.1016/j.cemconres.2018.02.016>.
- [60] Z. Shi, B. Lothenbach, The role of calcium on the formation of alkali-silica reaction products, *Cem. Concr. Res.* 126 (2019) 1–12, <https://doi.org/10.1016/j.cemconres.2019.105898>.
- [61] M. Thomas, The effect of supplementary cementing materials on alkali-silica reaction: a review, *Cem. Concr. Res.* 41 (2011) 1224–1231, <https://doi.org/10.1016/j.cemconres.2010.11.003>.
- [62] T. Ramlochan, M. Thomas, K.A. Gruber, Effect of metakaolin on alkali-silica reaction in concrete, *Cem. Concr. Res.* 30 (2000) 339–344, [https://doi.org/10.1016/S0008-8846\(99\)00261-6](https://doi.org/10.1016/S0008-8846(99)00261-6).
- [63] M. Shakoorkoskooie, M. Griffa, A. Leemann, R. Zboray, P. Lura, Alkali-silica reaction products and cracks: X-ray micro-tomography-based analysis of their spatial-temporal evolution at a mesoscale, *Cem. Concr. Res.* 150 (2021) 1–16, <https://doi.org/10.1016/j.cemconres.2021.106593>.